X-ray charge-density studies – a suitable probe for superconductivity?

Jan Langmann,[†] Hasan Kepenci,[†] Georg Eickerling,[*,†] Kilian Batke,[†] Anton Jesche,[‡] Mingyu Xu,[¶,§] Paul Canfield,[¶,§] and Wolfgang Scherer[*,†]

[†]*CPM, Institut für Physik, Universität Augsburg, 86159 Augsburg, Germany*

[‡]*Experimentalphysik VI, Zentrum für Elektronische Korrelation und Magnetismus, Institut für Physik, Universität Augsburg, 86159 Augsburg, Germany*

[¶]*The Ames Laboratory, Iowa State University, Ames, Iowa 50011, USA*

[§]*Department of Physics and Astronomy, Iowa State University, Ames, IA 50011, USA*

E-mail: georg.eickerling@uni-a.de; wolfgang.scherer@uni-a.de

Phone: +49 (0)821 598 3362; +49 (0)821 598 3350

Abstract

Case studies of 1T-$TiSe_2$ and $YBa_2Cu_3O_{7-\delta}$ have demonstrated that x-ray diffraction (XRD) studies can be used to trace even subtle structural phase transitions which are inherently connected with the onset of superconductivity in these benchmark systems. Yet, the utility of XRD in the investigation of superconductors like MgB_2 lacking an additional symmetry-breaking structural phase transition is not immediately evident. Even though, high-resolution powder XRD experiments on MgB_2 in combination with maximum entropy method (MEM) analyses hinted at differences between the electron density distributions at room temperature and 15 K, *i.e.* below the T_c of approx. 39 K. The high-resolution single-crystal XRD experiments in combination with multipolar refinements presented here can reproduce these results, but show that the observed temperature-dependent density changes are almost entirely due to a decrease of atomic displacement parameters as a natural consequence of reduced thermal vibration amplitude with decreasing temperature. Our investigations also shed new light on the presence or absence of magnesium vacancies in MgB_2 samples – a defect type claimed to control the superconducting properties of the compound. We propose that previous reports on the tendency of MgB_2 to form non-stoichiometric $Mg_{1-x}B_2$ phases ($1 - x \sim 0.95$) during high-temperature (HT) synthesis might result from the interpretation of XRD data of insufficient resolution and/or usage of inflexible refinement models. Indeed, advanced refinements based on an Extended Hansen-Coppens (EHC) multipolar model and high-resolution x-ray data, which consider explicitly the contraction of core and valence shells of the magnesium cations, do not provide any significant evidence for the formation of non-stoichiometric $Mg_{1-x}B_2$ phases during HT synthesis.

Introduction

When a crystal enters the superconducting state, its electronic structure is subjected to fundamental changes. In case of BCS superconductors, electrons are coupled into Cooper pairs by means of lattice vibrations.[1] This has profound effects on physical quantities probed

by spectroscopic methods. Examples are the superconducting gap as determined for example via tunneling and vibrational spectroscopy[2,3] or the Knight shift determined via nuclear magnetic resonance spectroscopy.[4]

It is not directly evident, however, whether the transition from the normal- to the superconducting state has significant effects on the (one-)electron density distribution as probed by x-ray diffraction (XRD) experiments. *A priori* the electron density distribution in a real crystal is affected by various factors such as chemical bonding as well as static and dynamic atomic displacements due to disorder and thermal motion. All of these factors are possibly subject to changes at the superconducting transition. But up to now, experimental evidence for differences between normal- and superconducting electron density distributions from XRD is rather sparse and inconclusive. This even holds for MgB_2 (see structural model in Fig. 1) as one of the superconducting benchmark systems characterized by graphite-like boron layers with intercalated Mg cations. Xue *et al.* reported an anomalous increase of powder XRD reflection intensities at $T_c^{onset} \approx 39$ K.[5,6] Yet, the authors only consider changes in the phonon spectrum as a potential cause for their observation and neglect other factors. Nishibori *et al.*, by contrast, propose a change in chemical bonding to occur between room temperature and 15 K.[7] Their statement is based on maximum entropy method (MEM) analyses of powder XRD data that show an increasing electron density at the B–B bond-critical point (BCP) from 0.9 $e{\cdot}$Å^{-3} to 1.0 $e{\cdot}$Å^{-3} at decreasing temperatures.[7] These BCPs represent saddle-points in the electron density distribution along the boron-boron bonds (indicated by blue spheres in Fig. 1). But as the MEM technique is model free and unable to differentiate between different causes of changes in the electron density distribution, a modification of thermal smearing might account for the observations of Nishibori *et al.* as well.

In this paper, we therefore use multipolar refinements of temperature-dependent XRD data of single-crystalline MgB_2 samples to detect potential electron density redistributions above and below T_c,[5,7] and to clarify their origin. In contrast to earlier efforts, the application of flexible multipolar models allows a decomposition of the total electron density

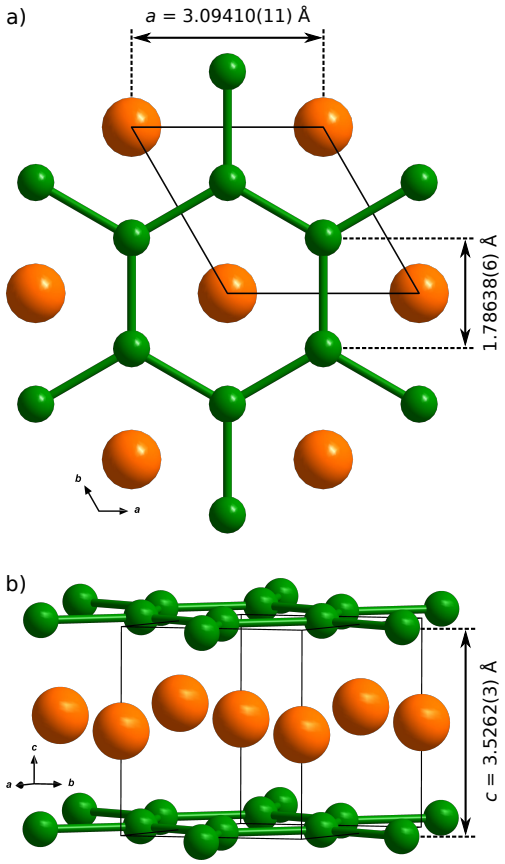

Figure 1: Ball-and-stick model of MgB_2 characterized by layers of magnesium (orange) and boron (green) atoms in the a-b plane (a) that alternate along the stacking direction c (b). Salient interatomic distances and lattice parameters at room temperature are specified.

distribution into different contributions, *i.e.* the sample composition, chemical bonding effects and displacements of atoms from their equilibrium positions due to static disorder or thermal motion.[8–10]

Methods

Single crystal growth

Single-crystalline samples of MgB_2 (crystal 1 and crystal 2; photographic images in Fig. S1 and Fig. S2 of the Supporting Information) were grown by a high-pressure and high-temperature synthesis similar to that described in Ref. 11 (see the Supporting Information for details).

Magnetization measurements

The temperature-dependent DC magnetization was determined for a MgB_2 single crystal (crystal 2) from the same batch as the one used in the XRD experiments (see Fig. S3 of the Supporting Information). Measurements were performed under zero-field cooling (ZFC) and field-cooling (FC) conditions in an applied field of $\mu_0 H = 10$ mT employing a QUANTUM-DESIGN MPMS3 SQUID magnetometer. Numerical volume integration of a crystal model created with the software APEX2[12] was used to obtain the sample volume for the calculation of the volume susceptibility $\chi(T)$. We have found $V = 2.3(1) \cdot 10^{-3}$ mm^3. The superconducting transition temperature was determined to $T_c = 37.5$ K (onset).

The ZFC value of $\chi(T)$ = -1.03 at $T = 2$ K corresponds to a superconducting volume fraction of close to 100 % that is overestimated due to neglecting demagnetization effects and the volume error. The FC $\chi(T)$ amounts to roughly 45 % of the ZFC value, which is larger than in previous studies (e.g. Ref. 6) and indicates a lower concentration of pinning centers.

XRD data collection and reduction

Two different setups were employed to collect the x-ray diffraction (XRD) data in this paper: An experiment at 100(2) K was performed on a BRUKER Smart-Apex diffractometer featuring a D8 goniometer, an INCOATEC AgK_α microfocus sealed-tube as x-ray source ($\lambda = 0.56087$ Å) and a standard OXFORD open-flow N_2 cooler (diffractometer 1).[13] Experiments at temperatures from room temperature down to sub-nitrogen cryogenic temperatures relied on a HUBER four-circle Eulerian cradle goniometer equipped with a DECTRIS Pilatus CdTe 300K pixel detector, an INCOATEC AgK_α microfocus sealed-tube x-ray source ($\lambda = 0.56087$ Å) and an ARS closed-cycle helium cryocooler with an outer and inner beryllium vacuum and radiation shield (diffractometer 2). Data collection at different temperatures was performed in direct sequence without sample re-orientation. Recorded Bragg intensities were evaluated using the `APEX2`[12] (diffractometer 1) or the `EVAL14` integration

programs[14,15] (diffractometer 2) and subjected to scaling and absorption corrections using the program SADABS.[16] More information on collection and processing of the XRD data can be found in the Supporting Information.

IAM and multipolar refinements

Independent atom model (IAM) and multipolar refinements were performed using the programs JANA2006[17] or JANA2020[17] (see the Supporting Information for information on local coordinate systems, refined parameters and residual electron density maps of all multipolar models employed in this paper). For better comparability of the results the construction of atomic electron densities $\rho_{\mathrm{at}}(\mathbf{r})$ and scattering factors was in all cases based on atomic wave functions for neutral reference atoms as implemented in the standard database of JANA2006/JANA2020.[17]

IAM refinements in this paper feature atomic scattering factors of neutral magnesium and boron atoms. The atomic scattering factor of magnesium was calculated using a configuration of $[1s^2,2s^2,2p^6](3s^2)$ with $[1s^2,2s^2,2p^6]$ defining the core and $(3s^2)$ the valence. For boron a $[1s^2](2s^1,2p^2)$ configuration was assumed.

To account for the expected charge transfer, in the Standard Hansen-Coppens (SHC) multipolar refinements the ζ-exponents for the valence radial function on magnesium was calculated from the s/p ratio of an $[1s^2](2s^2,2p^6)$ configuration. At the same time, the according s/p ratio of boron was still calculated from an $[1s^2](2s^1,2p^2)$ configuration. Starting values of the valence population parameters P_v were fixed to 8 for magnesium and 4 for boron to account for an ionic starting model composed of Mg^{2+} and B^{-}. Aspherical density deformations were described using one set of deformation functions centered at each of the atoms in the asymmetric unit of MgB_2 and employing maximum multipolar orders of $l_{\max} = 2$ (magnesium) and $l_{\max} = 3$ (boron). In contrast to earlier attempts,[18] our multipolar model allows for a free and simultaneous least-squares refinement of its parameters without the need for a manual variation of P_v(Mg) and P_v(B). This increases the likelihood of identifying

the global refinement minimum and results in a good fit to the available reflection intensities up to $(\sin\theta/\lambda)_{\max} = 1.3$ Å^{-1}.

Extended Hansen-Coppens (EHC) multipolar refinements were employed in a detailed investigation of the presence or absence of magnesium vacancies in our sample. Model parameters were determined on the basis of static theoretical structure factors for MgB_2 with a stoichiometric composition of 1 Mg : 2 B and experimental single-crystal XRD data collected at $T = 100(2)$ K ($(\sin\theta/\lambda)_{\max} = 1.6$ Å^{-1}). The spherical contributions to $\rho_{\mathrm{at}}(\mathbf{r})$ of the magnesium and boron atoms were represented by three shells with electronic configurations of $(1s^2)$ / $(2s^2,\ 2p^6)$ / $(3s^2)$ and $(1s^2)$ / $(2s^1)$ / $(2p^2)$, respectively. Additionally, one set of aspherical deformation functions with maximum multipolar order $l_{\max} = 4$ was employed for each of the atoms in the asymmetric unit of MgB_2. In the refinements of theoretical structure factors and experimental data, the number of varied parameters was increased in a stepwise manner: In a first step, the multipolar parameters were refined, while the magnesium occupation factor was kept at a fixed value of 1.0. Thereby, the core multipolar parameters were only varied in case of theoretical structure factors (T-EHCM1). In case of experimental data, the final core multipolar parameter values from T-EHCM1 were adopted, but the scale factor and the anisotropic (harmonic) ADPs of the magnesium and boron atom were varied (E-EHCM1). Then, the magnesium site occupation factor, the scale factor, the anisotropic ADPs, and the core and valence multipolar parameters (theoretical structure factors; T-EHCM2) or the valence multipolar parameters (experimental data; E-EHCM2) were relaxed in a joint refinement.

DFT calculations

Density functional theory (DFT) calculations for structure factor generation have been performed using the `Wien2k` suite of programs.[19,20] LAPW wave function calculations employing the PBE functional,[21,22] a k-point sampling mesh of size 25×25×19 and a $R_{mt}K_{max}$ parameter of 10.0 were performed using the lattice parameters and fractional coordinates obtained

from the x-ray diffraction study at room temperature (see above). Static structure factors up to a resolution limit of 6 $Å^{-1}$ have been calculated with the `lapw3` module. Lattice dynamic calculations via the finite-difference approach based on a 5×5×3 supercell have been performed employing `phonopy`[23] in combination with the `VASP`[24–27] code as force calculator. The PBE functional, a k-mesh sampling of 9×9×7 and an energy cut-off of 600 eV have been used throughout. The q-mesh sampling for the calculation of thermal displacement parameters was done on a 17×17×15 grid of points.

The calculation of dynamic structure factors was done with a locally modified version of the `DENPROP` code,[28] details of the implementation are given in Appendix C. Wave function data was taken from the `Wien2k` calculations described above. The numerical integration of the Stockholder atoms[29] was done on a Lebedev-Laikov grid[30] with 590 angular points while using 923 and 961 radial points between 0.0001 and 16 a.u. from the atomic position for Mg and B, respectively. Contributions to the Stockholder weights from an atomic cluster consisting of 2013 and 2031 atoms were included in the calculation for Mg and B, respectively. The numerical integration errors employing these parameters were of the order of 10^{-4} e for the $F(000)$, the (non-iterated) stockholder charges obtained from the partitioning of the total electron density distribution were $+0.2778$ e and -0.1389 e for Mg and B, respectively. Structure factors for different temperatures were calculated employing the according experimentally determined unit cell parameters and calculated ADP parameters (see Tab. S10 of the Supporting Information), respectively, while the stockholder atomic electron densities were kept fixed.

Results and discussion

Magnesium site occupancy

Model-free approaches for the analysis of x-ray diffraction (XRD) data like the maximum entropy method (MEM) do not require an explicit consideration of sample defects and provide

a crystal-averaged electron density distribution. To perform successful multipolar refinements, however, one needs to consider deviations from the ideal sample stoichiometry – a frequent defect type which might also occur in other superconducting compounds, *e.g.* $YBa_2Cu_3O_{7-\delta}$.[31–35] Such non-stoichiometric deviations can be determined by least-squares refinements of the respective atomic site occupation factors. Otherwise neglection of sample defects may result in false model parameters as demonstrated in the case study of B/C occupational disorder in ScB_2C_2 by Haas *et al.*[36] Therefore, we focus on this aspect first.

For MgB_2 there has been a long-lasting debate about the existence or absence of magnesium vacancies and how they control the physical and especially superconducting properties. Whereas a large number of authors argued in favor of the presence of magnesium vacancies up to approx. 5 % even in nominally stoichiometric samples,[18,37–43] others questioned any significant deviations from the ideal composition 1 Mg : 2 B.[44] Interestingly, most reports of magnesium vacancies relied on the refinement of magnesium site occupation factors using the independent-atom-model (IAM) to fit powder or single-crystal XRD data.[18,37,40,41,43] By contrast, magnesium site occupation factors derived from powder neutron diffraction experiments[44] showed no significant deviation from unity. This discrepancy may be due to the fact that the IAM approach does not account for charge transfer between ions, the presence of aspherical density deformations and deformations of the atomic core densities resulting from the latter two effects[45–48] which in turn affect the determination of precise sample compositions.[36] In case of the pseudo-Zintl phase MgB_2, strong valence charge transfer from the magnesium cations to the covalently bonded anionic boron network[18,40,49–54] may hamper the determination of magnesium occupation factors by standard XRD refinement techniques.[53]

To study this possible pitfall in more detail we performed IAM structural refinements using neutral-atom scattering factors (*i.e.* explicitly and erroneously *not* taking charge transfer effects into account) to model static theoretical structure factors of MgB_2. These were derived from periodic DFT calculations for stoichiometric MgB_2. Accordingly, they are not biased by the presence of vacancies, impurity atoms like carbon or other experimental

errors and thus provide an idealized test set (see Methods section). In analogy to the treatment of experimental XRD data, the scale factor, the anisotropic atomic displacement parameters (ADPs) for magnesium and boron and the occupation factor of the magnesium site were refined. Notably, this refinement strategy is not only chosen for consistency with experiment. Due to the structural simplicity of MgB_2 with only two atoms in the asymmetric unit the aforementioned parameters are highly interdependent, so that their simultaneous refinement is essential for the following results. Furthermore, the magnesium occupation factor and the scale factor are correlated via the the number of electrons per asymmetric unit. This requires us to focus our study on one type of sample defect (in our case the Mg site occupancy), as a simultaneous refinement of B/Mg site occupation factors and the scale factor under a electroneutrality constraint is not feasible for MgB_2.

Fig. 2a reveals the dependency of the obtained magnesium site occupancy (represented by filled circles) on the maximum reciprocal-space resolution $(\sin\theta/\lambda)_{\max}$ of the employed data set. The resolution-dependent development of all remaining refined parameters is available in Fig. S4 of the Supporting Information.

It can be recognized from Fig. 2a that IAM refinements result in false magnesium site occupancies especially in case of low reciprocal-space resolution. Accordingly, in the resolution range $(\sin\theta/\lambda)_{\max} \leq 0.8$ Å^{-1} that is usually employed for standard XRD experiments magnesium site occupancies of approx. 95 % are obtained. We note that this value is remarkably close to IAM-based site occupancies reported in the literature[18,37,40,41] suggesting that these results might also be affected by insufficient data resolution and the choice of an inflexible IAM to model the data. Fig. 2 also reveals that at significantly higher resolutions $(\sin\theta/\lambda)_{\max}$, the magnesium site occupancy increases and approaches a maximum value of 98 %, while the correct value of 100 % is never reached. An analogous asymptotic behavior of the refined magnesium site occupancy with increasing resolution can be observed for experimental single-crystal XRD data collected up to $(\sin\theta/\lambda)_{\max} = 1.6$ Å^{-1} (crystal 1; $T = 100(2)$ K; open circles in Fig. 2; for the resolution dependence of all refined parameters

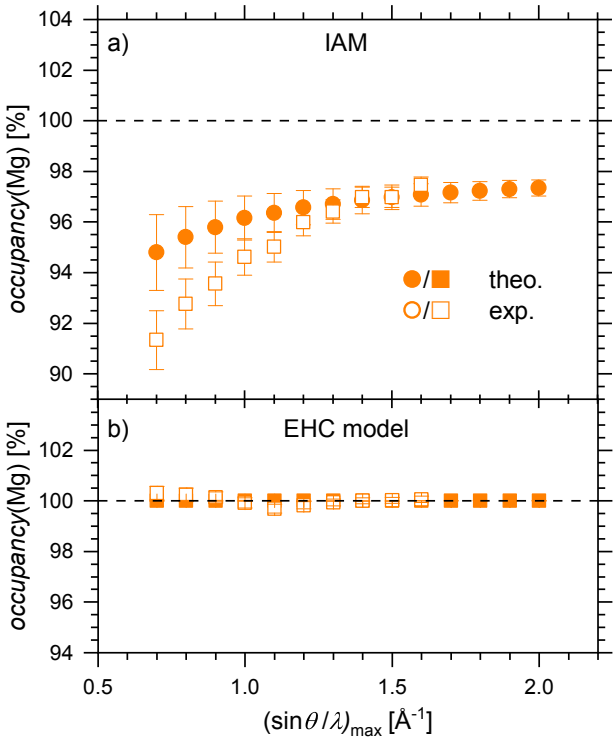

Figure 2: Variation of the magnesium site occupancy with increasing resolution $(\sin\theta/\lambda)_{\max}$ for different scenarios: using a) an IAM based on scattering factors of neutral atoms (circles) or b) an EHC model based on multipolar parameters (squares) to fit theoretical structure factors (filled symbols) or experimental single-crystal XRD data collected at $T = 100$ K (empty symbols) at a resolution $(\sin\theta/\lambda)_{\max} = 1.6$ Å^{-1}. In each case, the magnesium site occupation factor was refined simultaneously with the scale factor and the ADPs of the magnesium and boron atoms.

see Fig. S5 of the Supporting Information). Hence, our analysis suggests that false atomic site occupancies in compounds characterized by polar bonds and/or charged atoms are a natural consequence of using an independent atom model.

Multipolar models applied to high-resolution XRD data may overcome the inflexibility of the IAM by properly taking into account (*i*) charge transfer effects, (*ii*) aspherical density deformations due to chemical bonding, and (*iii*) the contraction or expansion of atomic shells (see Appendix A). The success of the multipolar approach in the determination of sample compositions was demonstrated by Haas *et al.*[36] In that study the coloring problem due to the mixed occupation of carbon/boron atomic sites in the borocarbide ScB_2C_2 could be resolved using high-resolution XRD data and a Standard Hansen-Coppens (SHC) multipolar model.[8] At ultra-high data resolutions ($\sin\theta/\lambda \gtrapprox 1.4$ Å^{-1}), however, also the charge-transfer between core and valence shells and core polarization effects due to chemical-bonding effects may need to be considered.[46,55] Otherwise, neglecting these core contraction/expansion or polarization effects in the SHC multipolar model can lead to drastically increased residual electron density features in the core-density region of atoms and may hamper the precise determination of ADPs[45,47,56] and/or atomic positions via so-called core-asphericity shifts.[48] In the Extended Hansen Coppens (EHC) multipolar model proposed for example by Batke *et al.*[46] and Fischer *et al.*[45,48] the frozen-core approximation of the SHC model is lifted, so that ultra-high-resolution XRD data can be fitted with good accuracy (see Appendix A).

In the following, we demonstrate the applicability of the multipolar approach to the problem of magnesium site occupancies in MgB_2. Similar to our evaluation of the IAM approach, we start with static structure factors from periodic DFT calculations for ideal MgB_2 lacking any magnesium vacancies (see Methods section). Thus, a magnesium site occupancy close to 100 % should be obtained in case of a successful modelling. In the least-squares refinement of multipolar models we used reflection data featuring the maximum achieved resolution $(\sin\theta/\lambda)_{\max} = 1.6$ Å^{-1} in our XRD experiments on MgB_2 (see Methods section). Core polarization effects present at $(\sin\theta/\lambda)_{\max} = 1.6$ Å^{-1} (see the resolution dependence

of the residual electron density at the magnesium position for IAM, SHC and EHC models in Fig. S9 of the Supporting Information) were taken into account by choosing a multipolar model at the EHC level. In a final step of the model refinement core and valence multipolar parameters, the scale factor, the anisotropic ADPs and the magnesium site occupation factor were varied jointly (denoted T-EHCM2 model; for more details, see the Methods section and the Supporting Information). The obtained magnesium site occupancy of 100.152(14) % is very close to 100 %, while the values of the scale factor (1.01007(19)) and the ADPs (U_{11}(Mg) = 0.000078(4) Å^2; U_{33}(Mg) = 0.000081(4) Å^2; U_{11}(B) = −0.000085(5) Å^2; U_{33}(B) = −0.000091(5) Å^2) show only minor deviations with respect to their expected values of unity and zero, respectively. Only a small dependency on the data resolution was observed hinting for a high robustness of the results (filled squares in Fig. 2b; resolution dependence of other refined parameters in Fig. S6 of the Supporting Information). Thus, the capability of the EHC approach to provide correct atomic site occupancies even in the presence of polar bonds or charged atoms appears drastically improved with respect to the IAM approach.

Next, we check for the presence or absence of magnesium vacancies in our MgB_2 sample by performing an EHC multipolar refinement on experimental single-crystal XRD data collected at T = 100(2) K (crystal 1; $(\sin\theta/\lambda)_{\max}$ = 1.6 Å^{-1}). Thereby, core multipolar parameters were fixed at their values obtained in the EHC model refinement of theoretical structure factors ($(\sin\theta/\lambda)_{\max}$ = 1.6 Å^{-1}). Again, a magnesium site occupancy close to 100 % was obtained (101.5(3) % at $(\sin\theta/\lambda)_{\max}$ = 1.6 Å^{-1}; E-EHCM2) with only a minor effect of changes in the data resolution (open rectangles in Fig. 2b; resolution dependence of other refined parameters in Fig. S7 of the Supporting Information). Thus, our combined experimental and theoretical EHC refinements rule out any significant evidence for the presence of magnesium vacancies in the investigated MgB_2 samples. Earlier reports on magnesium vacancies in the compound may thus be mainly attributed to shortcomings of the employed IAM approach and/or usage of low-resolution XRD data of MgB_2. Hence, this case study stresses the importance of using (*i*) a sufficiently high data resolution and (*ii*) appropriate

multipolar models in the data analysis, when reliable and accurate site occupancies need to be derived from x-ray diffraction data.

Temperature-dependent changes in the electron density distribution

We first focus on topological analyses of static electron density distributions as derived from an EHC multipolar refinement of XRD data collected at $T = 100(2)$ K ($\rho_{\mathrm{EHC}}(\mathbf{r})$; $(\sin\theta/\lambda)_{\mathrm{max}} = 1.6$ Å^{-1}; model E-EHCM1) and periodic DFT calculations using the Quantum Theory of Atoms in Molecules (QTAIM)[57,58] before we discuss potential changes induced by the onset of superconductivity. Maps of the Laplacian of the electron density, $\nabla^2\rho(\mathbf{r})$, in planes showing nearest-neighbor boron-boron and boron-magnesium contacts are given in Fig. 3 (topological characteristics and Laplacian maps for the other multipolar models in this paper are available in Tab. S9, Fig. S15 and Fig. S16 of the Supporting Information). In agreement with a description of MgB_2 as a pseudo-Zintl phase[49] and previous experimental[18,40,53,54] and theoretical results,[50–52] only the bond-critical point (BCP) at the midpoint of the B–B contact (#1 in Fig. 3) shows a large $\rho(\mathbf{r}_c)$ of 0.80 e·Å^{-3} [DFT: 0.82 e·Å^{-3}] and a strongly negative $\nabla^2\rho(\mathbf{r}_c)$ value of -3.30 e·Å^{-5} [DFT: -4.85 e·Å^{-5}] in line with the presence of covalent interactions. The magnesium-boron contact (CP #2 in Fig. 3b), by contrast, is characterized by rather electrostatic closed-shell interactions indicated by a small $\rho(\mathbf{r}_c)$ value of 0.19 e·Å^{-3} [DFT: 0.16 e·Å^{-3}] and a positive $\nabla^2\rho(\mathbf{r}_c)$ value of $+1.94$ e·Å^{-5} [DFT: $+1.92$ e·Å^{-5}].[1] This is also evident from the respective atomic charges of $+1.6$ e and -0.8 e [DFT: $+1.6$ e/-0.8 e] as a consequence of the pronounced charge transfer from the electropositive magnesium atoms towards the boron atoms which form the a graphene-type network characterized by delocalized π electrons.

On the basis of MEM analyses of powder XRD data Nishibori *et al.*[7] suggested that the chemical bonding situation in MgB_2 changes significantly upon cooling from room temper-

[1] In analogy to the results of the charge-density study by Tsirelson *et al.*[18] some of the Hessian eigenvalues of critical points #2 and #5 are close to zero (Fig. 3). Thus, the corresponding signatures of the critical points are topologically unstable (see also the Supporting Information).

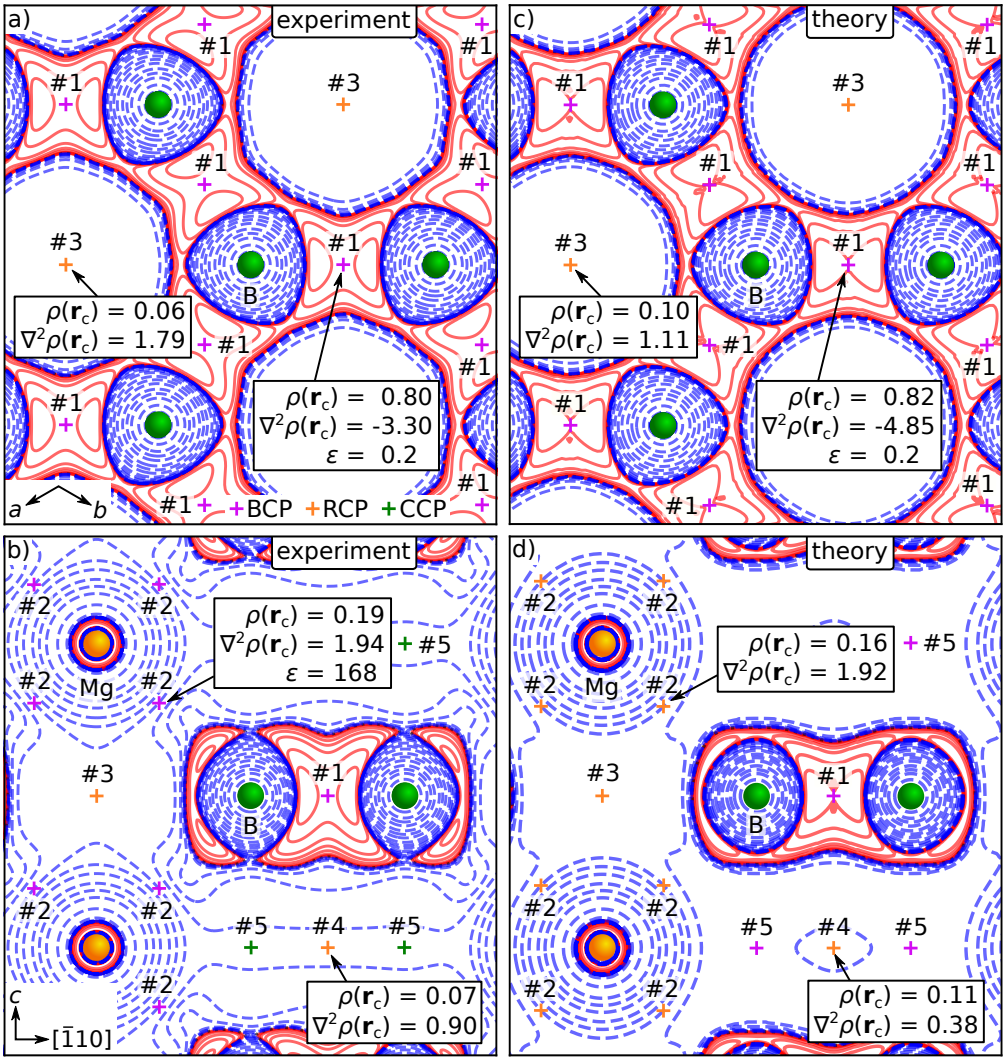

Figure 3: Maps of the Laplacian of the electron density, $\nabla^2\rho(\mathbf{r})$, in the boron network parallel to the *a*-*b* plane (a,c), and in a plane parallel to the c-axis enclosing the magnesium and boron atoms (b,d). The static $\rho(\mathbf{r})$ distributions were obtained from EHC model E-EHCM1 using experimental single-crystal XRD data (a,c; $T = 100$ K) and from periodic DFT calculations (b,d; see text). Contour lines are drawn for negative (solid red lines) and positive values of $\nabla^2\rho(\mathbf{r})$ (dashed blue lines) at levels of $\pm 2 \cdot 10^n$, $\pm 4 \cdot 10^n$, and $\pm 8 \cdot 10^n$ with $n \in \{-2, \ldots, 3\}$; $\rho(\mathbf{r}_c)$ values (in $e{\cdot}\text{Å}^{-3}$) and Laplacian $\nabla^2\rho(\mathbf{r}_c)$ values (in $e{\cdot}\text{Å}^{-5}$). The bond ellipticity ϵ values are specified at the locations of critical points (indicated by crosses). Their numbering refers to Tab. S9 in the Supporting Information.

ature to 15 K, *i.e.* a temperature below the superconducting T_c. According to the authors these electronic structure changes are clearly indicated by an increased density at the B–B BCP (1.0 $e{\cdot}\text{Å}^{-3}$ at 15 K compared to 0.9 $e{\cdot}\text{Å}^{-3}$ at RT) which results from a charge transfer from delocalized π to localized σ bonds in the hexagonal boron layers[7] (see the structural model in Fig. 1). However, the MEM analyses employed by Nishibori *et al.*[7] solely provide density distributions $\rho_{\text{MEM}}(\mathbf{r})$ that are compatible with observed structure factor amplitudes and maximize information entropy.[10,59,60] As such they only show the combined effect of density deformations due to chemical bonding as well as dynamic and static atomic displacements.[10] Hence, a definitive attribution of the observed electron density increase to one of these factors is not possible. To identify the origin and nature of the temperature-dependent density variation at the B-B BCPs we performed high-resolution charge density studies employing a single crystal (crystal 1) at various temperatures above and below the T_c. The according $T_c \approx 37.5$ K was determined from magnetic susceptibility studies of a single crystal (crystal 2) from the same synthesis batch. Our measurements relied on a low-temperature diffractometer setup featuring a closed-cycle helium cryocooler to reach sub-nitrogen cryogenic temperatures (further information in the Methods section and the Supporting Information). The employed cooling equipment puts restrictions on the possible goniometer settings, so that the available data resolution is reduced from $(\sin\theta/\lambda)_{\text{max}} = 1.6$ Å^{-1} to 1.3 Å^{-1}. Therefore, Standard Hansen-Coppens (SHC) multipolar models[8] with a fixed magnesium site occupancy of 100 % were refined against the low-temperature XRD data to maintain a high data-to-parameter ratio and to reduce potential parameter correlations (see Appendix A, Methods section and Supporting Information).

As a starting point, we compare the total temperature-dependent changes of the electron density distribution between 13.5 K and room-temperature (RT) as obtained by our SHC refinements with the $\rho_{\text{MEM}}(\mathbf{r})$ changes between 15 K and RT as observed by Nishibori *et al.*[7] To directly visualize the *modification* of the electron density distribution, we consider the total temperature-dependent difference electron density, $\Delta\rho_{\text{total}}(\mathbf{r})$, between 13.5 K and

RT (Fig. 4a and Fig. 4g) obtained by subtracting densities $\rho_{\rm o}(\mathbf{r}$, 13.5 K) and $\rho_{\rm o}(\mathbf{r}$, RT) from each other. Each of the individual densities $\rho_{\rm o}(\mathbf{r},T)$ is calculated by Fourier summation over the observed structure factor amplitudes at the respective temperature T (see Appendix B). Similar to $\rho_{\rm MEM}(\mathbf{r})$, but in contrast to the previously discussed model density $\rho_{\rm EHC}(\mathbf{r})$, each density $\rho_{\rm o}(\mathbf{r},T)$ reflects the *joint* effect of chemical bonding as well as static and dynamic atomic displacements on the electron density distribution at a specific temperature.

Fig. 4a and Fig. 4g show iso-contour maps of $\Delta\rho_{\rm total}(\mathbf{r})$ in planes parallel and perpendicular to the hexagonal boron layers in MgB_2. Complementary maps of the standard deviation of $\Delta\rho_{\rm total}(\mathbf{r})$ (see Appendix B for details on their generation) are given in Fig. 4b and Fig. 4h to ease the differentiation between significant and non-significant features. In fact, inspection of Fig. 4a and Fig. 4g reveals an increase of the electron density at the B–B BCP (#1 in Fig. 4) by 0.300 $e{\cdot}\text{Å}^{-3}$ and a decrease by 0.021 $e{\cdot}\text{Å}^{-3}$ at the B$\cdots$Mg BCP (#2 in Fig. 4) upon cooling from RT to 13.5 K. The identified density accumulation at the B–B BCP is in qualitative agreement with the increase of $\rho_{\rm MEM}(\mathbf{r})$ by 0.1 $e{\cdot}\text{Å}^{-3}$ between RT and 15 K reported by Nishibori *et al.*[7] Yet, these are not the strongest temperature-dependent changes pointed out by $\Delta\rho_{\rm total}(\mathbf{r})$: The maps in Fig. 4a and Fig. 4g are clearly dominated by atom-centered spherical features with a radial alternation of sign. At the atomic positions, $\Delta\rho_{\rm total}(\mathbf{r})$ is found to be strongly positive with values of 5.661 $e{\cdot}\text{Å}^{-3}$ for boron and 22.791 $e{\cdot}\text{Å}^{-3}$ for magnesium.

To proceed beyond the MEM level and to investigate the origin of the observed features we decompose $\Delta\rho_{\rm total}(\mathbf{r})$ into components according to

$$\Delta\rho_{\rm total}(\mathbf{r}) = \Delta\rho_{\rm latt}(\mathbf{r}) + \Delta\rho_{\rm ADP}(\mathbf{r}) + \Delta\rho_{\rm MP}(\mathbf{r}) + \Delta\rho_{\rm res}(\mathbf{r}) \qquad (1)$$

using Fourier summations over *observed* and/or *calculated* structure factor amplitudes from our multipolar models (see Appendix B). This procedure enables the visualization of the

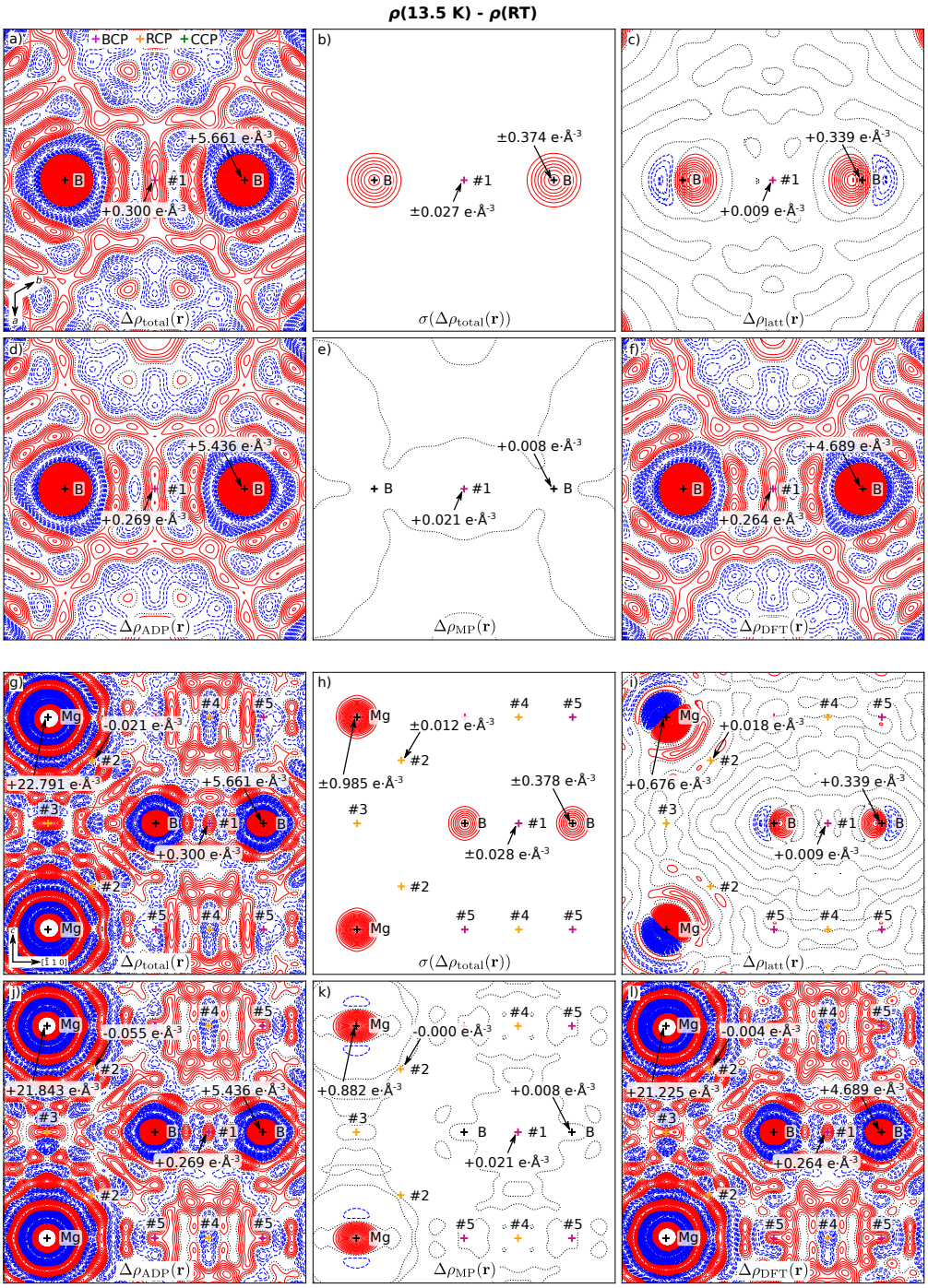

Figure 4: Iso-contour maps of differences between electron density distributions at 13.5 K and RT in planes parallel (a-f) and perpendicular to the hexagonal boron layers in MgB_2 (g-l). The standard deviation $\sigma(\Delta\rho_{\text{total}}(\mathbf{r}))$ of the total difference density $\Delta\rho_{\text{total}}(\mathbf{r})$ (a,g) has been specified in b) and h). It has been further decomposed into contributions from changes in the lattice parameters (c,i), the ADPs (d,j), and the multipolar parameters (MP; e,k). Standard DFT techniques can reproduce $\Delta\rho_{\text{total}}(\mathbf{r})$ without consideration of the superconducting transition (f,l; see text). Contour lines at positive (red; solid), zero (black; dotted) and negative values (blue; dashed) are equally spaced by increments of $\pm 0.05\ e{\cdot}\text{Å}^{-3}$. Crosses indicate the location of the QTAIM critical points introduced in Fig. 3.

individual difference density contributions of changes in (*i*) the lattice parameters ($\Delta\rho_{\mathrm{latt}}(\mathbf{r})$; Fig. 4c and Fig. 4i), (*ii*) the atomic displacement parameters (ADPs) ($\Delta\rho_{\mathrm{ADP}}(\mathbf{r})$; Fig. 4d and Fig. 4j), (*iii*) the multipolar parameters ($\Delta\rho_{\mathrm{MP}}(\mathbf{r})$; Fig. 4e and Fig. 4k), and (*iv*) residual changes ($\Delta\rho_{\mathrm{res}}(\mathbf{r})$) not captured by the employed multipolar models. It becomes evident that the lattice contraction between RT and 13.5 K leads to dipolar patterns centered at the atomic positions in $\Delta\rho_{\mathrm{latt}}(\mathbf{r})$ (Fig. 4c and Fig. 4i). But at the same time, the effect of a shrinkage in lattice parameters a and c on the density between the atomic positions is minimal (0.009 $e{\cdot}\mathrm{\AA}^{-3}$ at the B–B BCP and 0.018 $e{\cdot}\mathrm{\AA}^{-3}$ at the B$\cdots$Mg BCP). Density changes $\Delta\rho_{\mathrm{MP}}(\mathbf{r})$ (Fig. 4e and Fig. 4k) are connected to a variation of multipolar parameters (MP) and – if present – may indicate a modified chemical bonding situation in MgB_2 as proposed by Nishibori *et al.*[7] The contribution of $\Delta\rho_{\mathrm{MP}}(\mathbf{r})$ to $\Delta\rho_{\mathrm{total}}(\mathbf{r})$ is, however, even smaller than that of $\Delta\rho_{\mathrm{latt}}(\mathbf{r})$ (0.021 $e{\cdot}\mathrm{\AA}^{-3}$ at the B–B BCP and -0.000 $e{\cdot}\mathrm{\AA}^{-3}$ at the B$\cdots$Mg BCP). The only notable feature in maps of $\Delta\rho_{\mathrm{MP}}(\mathbf{r})$ are quadrupole-like patterns accumulating density at the positions of the magnesium atoms (Fig. 4k). Finally, maps Fig. 4d and Fig. 4j show density changes $\Delta\rho_{\mathrm{ADP}}(\mathbf{r})$ related to a temperature-dependent variation of ADPs. Their striking similarity to maps of $\Delta\rho_{\mathrm{total}}(\mathbf{r})$ (Fig. 4a and Fig. 4g) emphasizes that the large temperature difference between RT and 13.5 K renders the reduction of thermal smearing the most important source of temperature-dependent density changes (0.269 $e{\cdot}\mathrm{\AA}^{-3}$ at the B–B BCP and -0.055 $e{\cdot}\mathrm{\AA}^{-3}$ at the B$\cdots$Mg BCP). Not only the spherically alternating patterns at the atomic positions in $\Delta\rho_{\mathrm{total}}(\mathbf{r})$ are reproduced by $\Delta\rho_{\mathrm{ADP}}(\mathbf{r})$, but also most of the features in the inter-atomic region. Accordingly, the increase of $\Delta\rho_{\mathrm{total}}(\mathbf{r})$ at the B–B BCP by 0.300 $e{\cdot}\mathrm{\AA}^{-3}$ can be decomposed into contributions of 0.009 $e{\cdot}\mathrm{\AA}^{-3}$ ($\hat{=}$ 3.0 %) from $\Delta\rho_{\mathrm{latt}}(\mathbf{r})$, 0.021 $e{\cdot}\mathrm{\AA}^{-3}$ ($\hat{=}$ 7.0 %) from $\Delta\rho_{\mathrm{MP}}(\mathbf{r})$, and 0.269 $e{\cdot}\mathrm{\AA}^{-3}$ ($\hat{=}$ 89.7 %) from $\Delta\rho_{\mathrm{ADP}}(\mathbf{r})$. Small remaining contributions to $\Delta\rho_{\mathrm{total}}(\mathbf{r})$ that cannot be captured by the employed multipolar models and cannot be assigned to variations in lattice, MP or ADP parameters are contained in the residual difference density, $\Delta\rho_{\mathrm{res}}(\mathbf{r})$ ($\hat{=}$ 0.3 %; corresponding iso-contour maps are available in Fig. S17 of the Supporting Information).

Further evidence for the dominant role of thermal smearing is provided by the fact that standard DFT calculations without consideration of the superconducting transition can reproduce the maps of $\Delta\rho_{\mathrm{total}}(\mathbf{r})$ in Fig. 4a and Fig. 4g to a large extent: The maps of $\Delta\rho_{\mathrm{DFT}}(\mathbf{r})$ in Fig. 4f and Fig. 4l were generated ab-initio from *dynamic* theoretical structure factors ($(\sin\theta/\lambda)_{\mathrm{max}} = 1.3$ Å^{-1}; see the Methods section and Appendix C for details on the procedure) using lattice parameters at 13.5 K and RT as the only experimental input. At the location of the B–B BCP, $\Delta\rho_{\mathrm{DFT}}(\mathbf{r})$ amounts to 0.264 e·Å^{-3} comparing to 0.300 e·Å^{-3} in $\Delta\rho_{\mathrm{total}}(\mathbf{r})$ and 0.269 e·Å^{-3} in $\Delta\rho_{\mathrm{ADP}}(\mathbf{r})$.

To reduce the impact of thermal smearing and lattice shrinkage on $\Delta\rho_{\mathrm{total}}(\mathbf{r})$ and to increase the sensitivity for potential other changes during the superconducting transition, we performed additional single-crystal XRD experiments closely above (45 K) and below (25 K) the $T_{\mathrm{c}} \approx 37.5$ K of our MgB_2 sample. Resulting maps of $\Delta\rho_{\mathrm{total}}(\mathbf{r})$ with a reduced spacing of contour values (±0.01 e·Å^{-3} instead of ±0.05 e·Å^{-3}) are given in Fig. 5. It can be recognized that in spite of the reduced temperature window between 45 K and 25 K $\Delta\rho_{\mathrm{total}}(\mathbf{r})$ remains positive at the B–B BCP (#1 in Fig. 5). The absolute value of $\Delta\rho_{\mathrm{total}}(\mathbf{r})$ at this position (0.084 e·Å^{-3}; Fig. 5a), however, is significantly reduced with respect to the larger temperature window between RT and 13.5 K (0.300 e·Å^{-3}; Fig. 4a). In accordance with the closer spacing of measuring temperatures, the decomposition of $\Delta\rho_{\mathrm{total}}(\mathbf{r})$ at the B–B BCP yields only minor contributions from temperature-dependent changes in lattice parameters as described by $\Delta\rho_{\mathrm{latt}}(\mathbf{r})$ (0.000 e·Å^{-3} $\hat{=}$ 0.0 %; Fig. 5c) and thermal smearing as described by $\Delta\rho_{\mathrm{ADP}}(\mathbf{r})$ (0.008 e·Å^{-3} $\hat{=}$ 9.5 %; Fig. 5d). Nevertheless, inspection of the according map of $\Delta\rho_{\mathrm{MP}}(\mathbf{r})$ in Fig. 5e reveals that again the largest part of the difference density $\Delta\rho_{\mathrm{total}}(\mathbf{r})$ at the B–B BCP position cannot be attributed to changes in bonding-induced density deformations (0.020 e·Å^{-3} $\hat{=}$ 23.8 %). Instead, most of $\Delta\rho_{\mathrm{total}}(\mathbf{r})$ at the B–B BCP is absorbed by the residual difference density $\Delta\rho_{\mathrm{res}}(\mathbf{r})$ (0.056 e·Å^{-3} $\hat{=}$ 66.7 %; Fig. 5f) for which an assignment to a specific origin is not possible by means of the employed multipolar models. We note however, that the obtained value of $\Delta\rho_{\mathrm{res}}(\mathbf{r})$ at the B–B BCP

is below the three-fold standard deviation $\pm 0.060\ e{\cdot}\text{Å}^{-3}$ of the difference density $\Delta\rho_{\text{total}}(\mathbf{r})$ at the same position (Fig. 5b) and therefore close to the limit of detectability.

Prevalent features in the maps of $\Delta\rho_{\text{total}}(\mathbf{r})$ between 25 K and 45 K (Fig. 5a and Fig. 5g) are centered at the positions of magnesium and boron atoms. These can partly be modelled by a reduction of the (harmonic) ADPs in the multipolar models between 45 K and 25 K (see $\Delta\rho_{\text{ADP}}(\mathbf{r})$ in Fig. 5d and Fig. 5j). But non-trivial difference density patterns around the boron atom in the *a*-*b* plane and the magnesium atom in the $[\bar{1}10]$-*c* plane remain undescribed (see maps of $\Delta\rho_{\text{res}}(\mathbf{r})$ in Fig. 5f and Fig. 5l). This and a notable discrepancy between maps of $\Delta\rho_{\text{total}}(\mathbf{r})$ (Fig. 5a and Fig. 5g) and $\Delta\rho_{\text{DFT}}(\mathbf{r})$ (Fig. S18a and Fig. S18b) derived from DFT calculations considering only changes in harmonic thermal motion between 25 K and 45 K (see Fig. S18 of the Supporting Information) might indicate a minor modification of potential anharmonic contributions to the atomic displacements in MgB_2. Notably, anharmonicity of phonons in MgB_2 has been revealed in DFT studies by Liu *et al.*[61] and Yildirim *et al.*,[62] although the importance of this effect for the emergence of superconductivity in the compound remains controversial.[63–68] The anharmonic effects in our sample, however, are too small to be captured by anharmonic ADPs. Their inclusion into our multipolar models resulted in only insignificant Gram-Charlier coefficients up to fourth order.

Hence, in our single-crystal XRD studies we could identify the accumulation of additional electron density at the B–B BCP upon cooling across the superconducting T_c of MgB_2. This is in qualitative agreement with the temperature-dependent behavior of the density $\rho_{\text{MEM}}(\mathbf{r})$ obtained in previous MEM analyses of powder XRD data by Nishibori *et al.*[7] At the same time, our results do not support their hypothesis of a reorganization of bonding-induced density deformations as a primary source of the observed temperature-dependent density changes. Multipolar refinements of our XRD data in combination with DFT studies instead link density increases at the BCP positions in MgB_2 to a reduction of thermal smearing as a natural consequence of sample cooling.

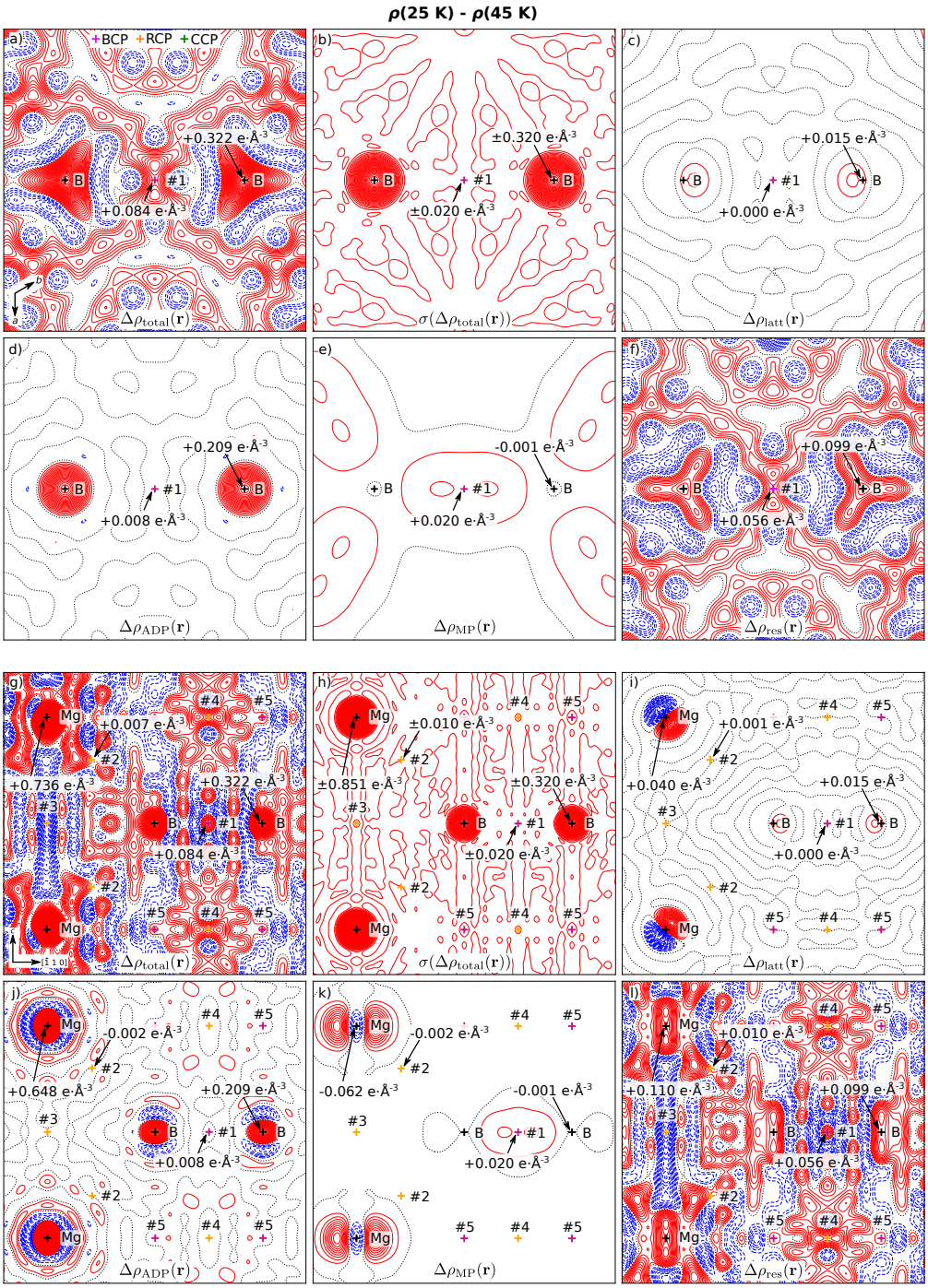

Figure 5: Iso-contour maps of differences between electron density distributions at 25 K and 45 K in planes parallel (a-f) and perpendicular to the hexagonal boron layers in MgB_2 (g-l). The standard deviation $\sigma(\Delta\rho_{\text{total}}(\mathbf{r}))$ of the total difference density $\Delta\rho_{\text{total}}(\mathbf{r})$ (a,g) has been specified in b) and h). Electron density differences have been decomposed into contributions from changes in the lattice parameters (c,i), the ADPs (d,j), and the multipolar parameters (MP; e,k) as well as residual changes not captured by the employed multipolar model (f,l; see text). Contour lines at positive (red; solid), zero (black; dotted) and negative values (blue; dashed) are equally spaced by increments of $\pm 0.01\ e{\cdot}\text{Å}^{-3}$. Crosses indicate the location of the QTAIM critical points introduced in Fig. 3.

Conclusion

To conclude, in our single-crystal x-ray diffraction (XRD) experiments we could not find evidence for a significant modification of the one-electron density distribution in MgB_2 directly related to the onset of superconductivity. With the help of multipolar refinements any marked electron density differences obtained from XRD experiments above and below the transition temperature T_c can be traced back to changes in thermal smearing. Their magnitude varies with the size of the temperature interval between the compared measurements and is correctly predicted by standard DFT techniques without the need for a consideration of superconductivity in MgB_2. Yet, the precise effect of a modified thermal smearing on the electron density distribution is by no means trivial. Namely, not only the electron density distribution close to the atomic positions of magnesium and boron is affected. Electron density may also be accumulated or depleted in the inter-atomic region away from the atomic nuclei. If XRD measurements at different temperatures are compared in model-free electron density studies, changes in thermal smearing may therefore be misinterpreted in terms of changes in chemical bonding.

But also simple model-based approaches turn out to be error prone, when applied to the pseudo-Zintl phase MgB_2. If electron density shifts due to chemical bonding and sizable charge transfer between magnesium and boron remain unmodeled in refinements of XRD data on the IAM level, wrong magnesium vacancy concentrations in the range of approx. 5 % may be obtained. By applying highly flexible Extended Hansen Coppens multipolar models[36,45,46,48] to high-resolution single-crystal XRD data we could demonstrate that our samples are fully stoichiometric with an insignificant vacancy concentration at the magnesium site. These findings have potential implications for the discussion about chemical control parameters of the superconductivity in MgB_2. Alternative explanations for systematic trends in the T_c with the weighed-in sample stoichiometry should be considered, *e.g.* the solution behavior of impurities in the starting materials magnesium and boron.[44]

Appendix A

In this paper, multipolar models at the Standard Hansen Coppens (SHC)[8,69] and the Extended Hansen Coppens (EHC)[45,46,48] level are employed. Generally, the flexibility of multipolar models is increased with respect to the IAM, as each atomic density contribution $\rho_{\mathrm{at}}(\mathbf{r})$ to the model density

$$\rho_{\mathrm{model}}(\mathbf{r}) = \sum_i \rho_{\mathrm{at},i}(\mathbf{r} - \mathbf{r}_i) \tag{2}$$

is decomposed into a sum over density contributions from a spherical core, a spherical valence and an aspherical valence deformation as

$$\begin{aligned}\rho_{\mathrm{at}}(\mathbf{r}) = & \underbrace{P_c \rho_c(r)}_{\text{(frozen) spherical core}} + \underbrace{P_v \kappa_v^3 \rho_v(\kappa_v, r)}_{\text{spherical valence}} \\ & + \underbrace{\sum_{l=0}^{l_{\max}} (\kappa'_{v,l})^3 R_l(\kappa'_{v,l}, r) \sum_{m=-l}^{l} P_{lm} d_{lm}(\theta, \phi)}_{\text{aspherical valence deformation}}\end{aligned} \tag{3}$$

Thereby, the population parameters P_c and P_v control the number of electrons attributed to the core and valence region. In multipolar refinements at the SHC level, the P_c parameter is usually kept at a fixed value, so that the spherical core density is effectively frozen. The spherical valence density, by contrast, is not fixed in order to account for charge transfer between the individual pseudo atoms via the P_v parameter and furthermore for contraction or expansion in radial direction by means of the κ_v parameter. Likewise, the radial part $R_l(\kappa'_{v,l}, r)$ of the aspherical valence deformation functions is contracted/expanded by means of the κ'_v parameter, while the asphericity of the valence density due to chemical bonding effects is controlled by the population parameters P_{lm} of the multipolar deformation density functions $d_{lm}(\theta, \phi)$.

The Extended Hansen-Coppens (EHC) approach systematically improves the SHC multipolar model by increasing its flexibility. An enhancement of the density fit can be accomplished by splitting the spherical core and spherical valence contribution to $\rho_{\mathrm{at}}(\mathbf{r})$ into different core and valence shells whose occupation and radial extent can be varied individually. This leads to the EHC model as for example proposed by Fischer *et al.*,[45] in which the pseudo-atom densities are written as

$$\begin{aligned}\rho_{\mathrm{at}}(\mathbf{r}) = & \underbrace{P_{1,c}\kappa_{1,c}^3\rho_{1,c}(\kappa_{1,c},r) + P_{2,c}\kappa_{2,c}^3\rho_{2,c}(\kappa_{2,c},r) + \cdots}_{\text{spherical core shells}} \\ & + \underbrace{P_{1,v}\kappa_{1,v}^3\rho_{1,v}(\kappa_{1,v},r) + P_{2,v}\kappa_{2,v}^3\rho_{2,v}(\kappa_{2,v},r) + \cdots}_{\text{spherical valence shells}} \\ & + \underbrace{\sum_{l=0}^{l_{\max}} (\kappa_v')^3 R_l(\kappa_v',r) \sum_{m=-l}^{l} P_{v,lm} d_{lm}(\theta,\phi)}_{\text{aspherical valence deformation}} \end{aligned} \tag{4}$$

A further improvement of model flexibility beyond the currently discussed level may be achieved by taking into account aspherical core polarizations,[55] as has been demonstrated for example by Fischer *et al.* in a recent experimental x-ray charge-density study of α-boron.[48]

Appendix B

In our analysis of temperature-dependent changes to the electron density distribution we focus on differences between observed ($\rho_{\mathrm{o}}(\mathbf{r})$) or calculated electron density distributions ($\rho_{\mathrm{c}}(\mathbf{r})$). This allows us to trace the origin of temperature-dependent changes by decomposing the total density difference into contributions from changes of (*i*) lattice parameters, (*ii*) atomic displacement parameters (ADPs), (*iii*) multipolar parameters and (*iv*) residual factors. Both, $\rho_{\mathrm{o}}(\mathbf{r})$ and $\rho_{\mathrm{c}}(\mathbf{r})$, are obtained from Fourier summations over all measured reflections $\mathbf{h}$ and take into account the limited experimental resolution. This, however, does

not lead to serious Fourier truncation errors, as only differences between densities $\rho_{\rm o}(\mathbf{r})$ or $\rho_{\rm c}(\mathbf{r})$ are considered in the following. The quantity

$$\rho_{\rm o}(\mathbf{r}) = \frac{s}{V} \sum_{\mathbf{h}} |F_{\mathbf{h}}^{\rm o}| \exp\left(-2\pi i \mathbf{h}\cdot\mathbf{r} + i\varphi_{\mathbf{h}}^{\rm c}\right) \tag{5}$$

(V: unit cell volume; s: scale factor) is computed from observed structure factor amplitudes $|F_{\mathbf{h}}^{\rm o}|$, *i.e.* the square roots of the measured reflection intensities. We note that due to the lack of observed structure factor phases $\varphi_{\mathbf{h}}^{\rm o}$ calculated phases $\varphi_{\mathbf{h}}^{\rm c}$ have to be used in the computation of both $\rho_{\rm o}(\mathbf{r})$ and $\rho_{\rm c}(\mathbf{r})$. The usage of $\varphi_{\mathbf{h}}^{\rm c}$ in Eq. (5), however, represents no approximation, since (*i*) the structure of MgB_2 is centro-symmetric. Hence, the phase angles are limited to values of 0 and π, which again (*ii*) are controlled by the fixed fractional coordinates of magnesium and boron atoms on special positions in the MgB_2 unit cell.

Similar to the electron density distribution from a MEM analysis, $\rho_{\rm o}(\mathbf{r})$ contains the joint effects of chemical bonding, and static or dynamic atomic displacements on the electron density distribution. It is also affected by experimental noise. The quantity

$$\rho_{\rm c}(\mathbf{r}) = \frac{1}{V} \sum_{\mathbf{h}} |F_{\mathbf{h}}^{\rm c}| \exp\left(-2\pi i \mathbf{h}\cdot\mathbf{r} + i\varphi_{\mathbf{h}}^{\rm c}\right) \tag{6}$$

is computed from structure factor amplitudes $|F_{\mathbf{h}}^{\rm c}|$ calculated in our case on the basis of the respective multipolar model. The individual model parameters determine to which degree $\rho_{\rm c}(\mathbf{r})$ is affected by charge transfer, chemical density deformations as well as static and dynamic atomic displacements. Accordingly, we can systematically study the influence of temperature-dependent changes in (*i*) lattice, (*ii*) thermal and (*iii*) multipolar parameters on the electronic structure my mapping the *difference* between electron density distributions observed at different temperatures.

To simplify the following discussion, we introduce a shorthand notation to indicate the

employed parameters in the generation of $\rho_{\mathrm{o}}(\mathbf{r})$ or $\rho_{\mathrm{c}}(\mathbf{r})$ maps. Our analysis showed that the $\rho_{\mathrm{o}}(\mathbf{r})$ maps depend not only on the structure factor amplitudes $|F_{\mathbf{h}}^{\mathrm{o}}|$, but also the lattice parameters (latt) of MgB_2 at a specific temperature. The temperature, at which $|F_{\mathbf{h}}^{\mathrm{o}}|$ and lattice parameters were determined, will from now on be indicated by specific superscripts in front of and behind the ρ symbol:

$$ {}^{|F_{\mathbf{h}}^{\mathrm{o}}|}\rho_{\mathrm{o}}^{\mathrm{latt}} \tag{7} $$

On the other hand, the $\rho_{\mathrm{c}}(\mathbf{r})$ maps depend on the ADPs, the multipolar parameters (MP) and the lattice parameters in the underlying multipolar model at a specific temperature. The multipolar models, from which the individual parameters were derived, are indicated by superscripts or subscripts grouped around the ρ symbol:

$$ {}^{\mathrm{ADP}}_{\mathrm{MP}}\rho_{\mathrm{c}}^{\mathrm{latt}} \tag{8} $$

A specific multipolar model is thereby characterized by the measuring temperature of its underlying XRD data set. We emphasize that parameters from different data sets or models may be combined. For example, a $\rho_{\mathrm{c}}(\mathbf{r})$ map may be based on lattice and ADP parameters pertaining to a temperature of 13.5 K and multipolar parameters pertaining to room temperature.

To obtain the total electron density difference between two measuring temperatures T_1 and T_2 ($T_1 < T_2$), we generate observed density maps $\rho_{\mathrm{o}}(\mathbf{r})$ from XRD data sets collected at T_1 and T_2. Thereby, the lattice parameters and structure factor amplitudes $|F_{\mathbf{h}}^{\mathrm{o}}|$ at the respective temperatures are used. The resulting maps are subtracted from each other:

$$\Delta\rho_{\mathrm{total}}(\mathbf{r}) = {}^{T_1}\rho_{\mathrm{o}}^{T_1}(\mathbf{r}) - {}^{T_2}\rho_{\mathrm{o}}^{T_2}(\mathbf{r}) \tag{9}$$

Changes solely due to a variation of lattice parameters are also accessible from the differences between two $\rho_{\mathrm{o}}(\mathbf{r})$ maps. In that case the difference maps are generated using the same $|F_{\mathbf{h}}^{\mathrm{o}}|$ values corresponding to the higher temperature T_2, but different lattice parameters corresponding to the lower temperature T_1 and the higher temperature T_2, respectively:

$$\Delta\rho_{\mathrm{latt}}(\mathbf{r}) = {}^{T_2}\rho_{\mathrm{o}}^{T_1}(\mathbf{r}) - {}^{T_2}\rho_{\mathrm{o}}^{T_2}(\mathbf{r}) \tag{10}$$

It is important to note that the choice of origin in the comparison of $\rho_{\mathrm{o}}(\mathbf{r})$ or $\rho_{\mathrm{c}}(\mathbf{r})$ maps with differing lattice parameters is non-trivial. To ensure consistent results the position of a B–B BCP was used as a reference point in the generation of difference density maps.

All remaining control parameters which influence the density distribution in MgB_2 can be studied by analysis of $\rho_{\mathrm{c}}(\mathbf{r})$ as obtained from our multipolar models. We thereby fix the lattice parameters to their values at the lower temperature T_1, since the effects of changes in the unit cell dimensions on the density already have been extracted via Eq. (10). In that case, the contribution of changes in the ADP parameters $\Delta\rho_{\mathrm{ADP}}(\mathbf{r})$ becomes visible, when $\rho_{\mathrm{c}}(\mathbf{r})$ maps for (i) a model with multipolar (MP) parameters corresponding to T_2 and ADPs corresponding to T_1 and (ii) a model with MP parameters and ADPs corresponding to T_2 are subtracted from each other:

$$\Delta\rho_{\mathrm{ADP}}(\mathbf{r}) = {}^{T_1}_{T_2}\rho_{\mathrm{c}}^{T_1}(\mathbf{r}) - {}^{T_2}_{T_2}\rho_{\mathrm{c}}^{T_1}(\mathbf{r}) \tag{11}$$

The contribution of changes in the MP parameters $\Delta\rho_{\mathrm{MP}}(\mathbf{r})$ is then revealed by subtract-

ing $\rho_{\mathrm{c}}(\mathbf{r})$ maps for (i) a model with ADPs and MP parameters corresponding to T_1 and (ii) a model with ADPs corresponding to T_1 and MP parameters corresponding to T_2 from each other.

$$\Delta\rho_{\mathrm{MP}}(\mathbf{r}) = {}^{T_1}_{T_1}\rho_{\mathrm{c}}^{T_1}(\mathbf{r}) - {}^{T_1}_{T_2}\rho_{\mathrm{c}}^{T_1}(\mathbf{r}) \tag{12}$$

All residual contributions to $\Delta\rho_{\mathrm{total}}(\mathbf{r})$ not captured by our multipolar models are contained in

$$\Delta\rho_{\mathrm{res}}(\mathbf{r}) = \Delta\rho_{\mathrm{total}}(\mathbf{r}) - \Delta\rho_{\mathrm{latt}}(\mathbf{r}) - \Delta\rho_{\mathrm{ADP}}(\mathbf{r}) - \Delta\rho_{\mathrm{MP}}(\mathbf{r}) \tag{13}$$

To assess the significance of features in $\Delta\rho_{\mathrm{total}}(\mathbf{r})$ or its underlying contributions, the underlying error needs to be known. Therefore, we generated maps of the standard deviation $\sigma(\Delta\rho_{\mathrm{total}}(\mathbf{r}))$ over two thousand $\Delta\rho_{\mathrm{total}}(\mathbf{r})$ maps generated with pseudo random numbers from the random module in NumPy[70] added to the values of the structure factor amplitude $|F_{\mathbf{h}}^{\mathrm{o}}|$ and scale factor s. Employed pseudo random numbers x follow normal distributions, whereby the probability density functions

$$p(x) = \frac{1}{\sqrt{2\pi\sigma^2}} \exp\left[-\frac{(x-\mu)^2}{2\sigma^2}\right] \tag{14}$$

are determined individually for each $|F_{\mathbf{h}}^{\mathrm{o}}|$ or s using a mean μ of 0 and a standard deviation σ equal to the respective estimated standard deviation.

Appendix C

The generation of the $\Delta\rho_{\mathrm{DFT}}(\mathbf{r})$ maps requires the calculation of dynamic structure factors from DFT calculations. The folding of a calculated static scattering factor $F_{\mathbf{h}}$ with a Debye-Waller factor obtained from an atomic ADP is a trivial step for one-atomic structures like Diamond. In contrast, compounds with more than one atom in the asymmetric unit such as MgB_2 require the decomposition of the total crystal electron density $\rho_{\mathrm{total,stat}}(\mathbf{r})$ into atomic contributions $\rho_i(\mathbf{r})$ prior to the folding with the probability density function $P(\mathbf{u})$ according to

$$\rho_{i,\mathrm{dyn}}(\mathbf{r}) = \int_{-\infty}^{\infty} \rho_{i,\mathrm{stat}}(\mathbf{r}-\mathbf{u})P(\mathbf{u}) \tag{15}$$

where $P(\mathbf{u})$ is the probability of atom i being displaced by $\mathbf{u}$ from its rest position and the Fourier-Transform of $P(\mathbf{u})$ is the Debye Waller factor $Q(\mathbf{h})$.

We have implemented this folding process into a locally modified version of the `DENPROP` code,[28] which for this purpose has been interfaced to solid-state programs such as `WIEN2K`.[19,20] Some details of this implementation are outlined in the following.

`DENPROP` can be used to calculate static x-ray structure factors from molecular wave functions represented in a Gaussian-type (GTO) or Slater-type (STO) basis set. In the former case the according Fourier-Transforms can be calculated analytically, whereas the calculation needs to be performed numerically in the latter case. But while the Fourier-Transform of an atom centered GTO basis function is thus readily calculated, the separation of the two-center terms into atomic contributions needs to be addressed properly (for an example, see the according implementation in the `CRYSTAL` code[71,72]).

The numerical approach implemented in `DENPROP` for the STO basis sets does not suffer from such ambiguities, but on the other hand requires sufficiently accurate integration grids. These are obtained by an atomic partitioning of the total electron density, for example via the

(iterative or non-iterative) stockholder approach. The resulting atomic densities $\rho_{i,\mathrm{stat}}(\mathbf{r})$ can then be accurately integrated on standard Lebedev-Laikov grids, thus yielding static atomic scattering factor contributions $f_{i,\mathrm{stat}}(\mathbf{h})$ which are finally summed up to the $F_{\mathrm{DFT,stat}}(\mathbf{h})$.

As this procedure intrinsically produces atomic densities and subsequently atomic scattering factors of the stockholder atoms from a total electron density distribution, we added a routine for the folding of the $f_{i,\mathrm{stat}}(\mathbf{h})$ with the according $Q(\mathbf{h})$ calculated from user provided isotropic or anisotropic ADPs. To generalize the data-input format and thus allow for calculation of dynamical structure factors also for solid state compounds represented for example in a plane wave basis, we further generalized the routine providing $\rho_{\mathrm{total,stat}}(\mathbf{r})$. In a first step all points of the atomic radial and angular integration grids are generated in Cartesian (x,y,z) format. This list of points can subsequently be used as input for any code capable of providing the total electron density of the system under investigation at a given point in space. Instead of being calculated solely from databases of atomic wave functions in GTO or STO format, the neutral atom reference electron density for the stockholder partitioning can now also be directly supplied by the user. For the present study we employed the atomic radial electron densities from which the `WIEN2k` code constructs the first-guess crystal density for the SCF calculation, while the total electron density of MgB_2 was calculated from the `Wien2k` LAPW wave function at the pre-generated list of points by the `CRITIC` code.[73,74] Contrary to the molecular case, were the number of atoms which need to be considered in the final integration step is simply defined by the number of atoms in the molecule (when assuming that the chosen pseudo unit cell is large enough for intermolecular interactions to be negligible), in solids the numerical accuracy critically depends on the definition of an sufficiently large atomic cluster surrounding the individual atom to be integrated. Our tests have shown, that a cut-off radius of 15 Å is usually sufficient for the generation of this cluster.

In summary, our generalized implementation allows for the generation of dynamic structure factors for a broad variety of use-cases, ranging for example[75] from fully relativistic

four-component calculations on molecules with the `DIRAC` code[76] to all-electron solid state calculations employing full-potential LAPW codes such as `Wien2k` or `ELK`.[77]

Acknowledgement

Work done at Ames Laboratory (MYX and PCC, growth of single crystalline MgB_2) was supported by the U.S. Department of Energy, Office of Basic Energy Science, Division of Materials Sciences and Engineering. Ames Laboratory is operated for the U.S. Department of Energy by Iowa State University under Contract No. DE-AC02-07CH11358.

Supporting Information Available

The following files are available free of charge.

- supporting.pdf: Supporting Information with details on the synthesis and crystal growth, investigated samples, the collection and processing of XRD data and the refined SHC and EHC multipolar models as well as a table of salient ab-initio ADP values and additional maps illustrating the decomposition of temperature-dependent changes in the electron density distribution.

References

(1) Alexandrov, A. S. *Theory of Superconductivity*, 1st ed.; Institute of Physics Publishing: Bristol, 2003; Chapter 2, pp 33–72.

(2) Poole, C. P.; Prozorov, R.; Farach, H. A.; Creswick, R. J. *Superconductivity*, 3rd ed.; Elsevier: Amsterdam, 2014; Chapter 13, pp 531–532.

(3) Poole, C. P.; Prozorov, R.; Farach, H. A.; Creswick, R. J. *Superconductivity*, 3rd ed.; Elsevier: Amsterdam, 2014; Chapter 14, pp 624–631.

(4) Poole, C. P.; Prozorov, R.; Farach, H. A.; Creswick, R. J. *Superconductivity*, 3rd ed.; Elsevier: Amsterdam, 2014; Chapter 14, pp 591–595.

(5) Xue, Y.; Asada, S.; Hosomichi, A.; Naher, S.; Xue, J.; Kaneko, H.; Suzuki, H.; Muranaka, T.; Akimitsu, J. X-ray Diffraction Study of MgB_2 at Low Temperatures. *J. Low Temp. Phys.* **2005**, *138*, 1105–1115.

(6) Nagamatsu, J.; Nakagawa, N.; Muranaka, T.; Zenitani, Y.; Akimitsu, J. Superconductivity at 39 K in magnesium diboride. *Nature* **2001**, *410*, 63–64.

(7) Nishibori, E.; Takata, M.; Sakata, M.; Tanaka, H.; Muranaka, T.; Akimitsu, J. Bonding Nature in MgB_2. *J. Phys. Soc. Jpn.* **2001**, *70*, 2252–2254.

(8) Hansen, N. K.; Coppens, P. Testing aspherical atom refinements on small-molecule data sets. *Acta Cryst.* **1978**, *A34*, 909–921.

(9) Coppens, P. *X-ray Charge Densities and Chemical Bonding*; International Union of Crystallography: Chester, Chapter 3.2, pp 59–71.

(10) Gatti, C.; Macchi, P. *Modern Charge-Density Analysis*, 1st ed.; Springer: Dordrecht, 2012; Chapter 1, pp 1–78.

(11) Louden, E. R.; Manni, S.; Zandt, J. E. V.; Leishman, A. W. D.; Taufour, V.; Bud'ko, S. L.; DeBeer-Schmitt, L.; Honecker, D.; Dewhurst, C. D.; Canfield, P. C. et al. Effects of magnetic and non-magnetic doping on the vortex lattice in MgB_2. *Journal of Applied Crystallography* **2022**, *55*, 693–701.

(12) Bruker (2012), *APEX2*. Bruker AXS Inc., Madison, Wisconsin, USA.

(13) Cosier, J.; Glazer, A. M. A nitrogen-gas-stream cryostat for general X-ray diffraction studies. *J. Appl. Cryst.* **1986**, *19*, 105–107.

(14) Duisenberg, A. J. M. Indexing in single-crystal diffractometry with an obstinate list of reflections. *J. Appl. Cryst.* **1992**, *25*, 92–96.

(15) Duisenberg, A. J. M.; Kroon-Batenburg, L. M. J.; Schreurs, A. M. M. An intensity evaluation method: *EVAL*-14. *J. Appl. Cryst.* **2003**, *36*, 220–229.

(16) Krause, L.; Herbst-Irmer, R.; Sheldrick, G. M.; Stalke, D. Comparison of silver and molybdenum microfocus X-ray sources for single-crystal structure determination. *J. Appl. Cryst.* **2015**, *48*, 3–10.

(17) Petříček, V.; Dušek, M.; Palatinus, L. Crystallographic Computing System JANA2006: General features. *Z. Kristallogr. Cryst. Mater.* **2014**, *229*, 345–352.

(18) Tsirelson, V.; Stash, A.; Kohout, M.; Rosner, H.; Mori, H.; Sato, S.; Lee, S.; Yamamoto, A.; Tajima, S.; Grin, Y. Features of the electron density in magnesium diboride: reconstruction from X-ray diffraction data and comparison with TB-LMTO and FPLO calculations. *Acta Cryst.* **2003**, *B59*, 575–583.

(19) Blaha, P.; Schwarz, K.; Tran, F.; Laskowski, R.; Madsen, G. K. H.; Marks, L. D. WIEN2k: An APW+lo program for calculating the properties of solids. *J. Chem. Phys.* **2020**, *152*, 074101.

(20) Blaha, P.; Schwarz, K.; Madsen, G. K. H.; Kvasnicka, D.; Luitz, J. *WIEN2k, An Augmented Plane Wave + Local Orbitals Program for Calculating Crystal Properties (Karlheinz Schwarz, Techn. Universität Wien, Austria), 2018. ISBN 3-9501031-1-2*; 2018.

(21) Perdew, J. P.; Burke, K.; Ernzerhof, M. Generalized Gradient Approximation Made Simple. *Physical Review Letters* **1996**, *77*, 3865—3868.

(22) Perdew, J. P.; Burke, K.; Ernzerhof, M. Generalized Gradient Approximation Made Simple – Errata. *Physical Review Letters* **1997**, *78*, 1396—-1396.

(23) Togo, A.; Tanaka, I. First principles phonon calculations in materials science. *Scr. Mater.* **2015**, *108*, 1–5.

(24) Kresse, G.; Furthmüller, J. Efficiency of ab-initio total energy calculations for metals and semiconductors using a plane-wave basis set. *Comput. Mater. Sci.* **1996**, *6*, 15–50.

(25) Kresse, G.; Furthmüller, J. Efficient iterative schemes for *ab initio* total-energy calculations using a plane-wave basis set. *Phys. Rev. B* **1996**, *54*, 11169–11186.

(26) Kresse, G.; Hafner, J. *Ab initio* molecular-dynamics simulation of the liquid-metal-amorphous-semiconductor transition in germanium. *Phys. Rev. B* **1994**, *49*, 14251–14269.

(27) Kresse, G.; Hafner, J. *Ab initio* molecular dynamics for liquid metals. *Phys. Rev. B* **1993**, *47*, 558–561.

(28) Volkov, A.; Koritsanszky, T.; Chodkiewicz, M.; King, H. F. On the basis-set dependence of local and integrated electron density properties: Application of a new computer program for quantum-chemical density analysis. *J. Comput. Chem.* **2009**, *30*, 1379–1391.

(29) Hirshfeld, F. L. Bonded-atom fragments for describing molecular charge densities. *Theor. Chem. Acc.* **1977**, *44*, 129–138.

(30) Lebedev, V. I.; Laikov, D. N. A Quadrature Formula for the Sphere of the 131st Algebraic Order of Accuracy. *Dokl. Math.* **1999**, *59*, 477–548.

(31) Jorgensen, J. D.; Veal, B. W.; Kwok, W. K.; Crabtree, G. W.; Umezawa, A.; Nowicki, L. J.; Paulikas, A. P. Structural and superconducting properties of orthorhombic and tetragonal $YBa_2Cu_3O_{7-x}$: The effect of oxygen stoichiometry and ordering on superconductivity. *Phys. Rev. B* **1987**, *36*, 5731–5734.

(32) Jorgensen, J. D.; Shaked, H.; Hinks, D. G.; Dabrowski, B.; Veal, B. W.; Paulikas, A. P.; Nowicki, L. J.; Crabtree, G. W.; Kwok, W. K.; Nunez, L. H. et al. Oxygen vacancy ordering and superconductivity in $YBa_2Cu_3O_{7-x}$. *Physica C* **1988**, *153–155*, 578–581.

(33) Dharwadkar, S. R.; Jakkal, V. S.; Yakhmi, J. V.; Gopalakrishnan, I. K.; Iyer, R. M. X-ray diffraction coupled thermogravimetric investigations of $YBa_2Cu_3O_{7-x}$. *Solid State Commun.* **1987**, *64*, 1429–1433.

(34) Beno, M. A.; Soderholm, L.; Capone, D. W.; Hinks, D. G.; Jorgensen, J. D.; Grace, J. D.; Schuller, I. K.; Segre, C. U.; Zhang, K. Structure of the single-phase high-temperature superconductor $YBa_2Cu_3O_{7-\delta}$. *Appl. Phys. Lett.* **1987**, *51*, 57–59.

(35) Manthiram, A.; Swinnea, J. S.; Sui, Z. T.; Steinfink, H.; Goodenough, J. B. The Influence of Oxygen Variation on the Crystal Structure and Phase Composition of the Superconductor $YBa_2Cu_3O_{7-x}$. *J. Am. Chem. Soc.* **1987**, *109*, 6667–6669.

(36) Haas, C. D.; Fischer, A.; Hauf, C.; Wieser, C.; Schmidt, A. P.; Eickerling, G.; Scheidt, E.-W.; Schiffmann, J. G.; Reckeweg, O.; DiSalvo, F. J. et al. The Color of the Elements: A Combined Experimental and Theoretical Electron Density Study of ScB_2C_2. *Angew. Chem. - Int. Ed.* **2019**, *58*, 2360–2364.

(37) Serquis, A.; Zhu, Y. T.; Peterson, E. J.; Coulter, J. Y.; Peterson, D. E.; Mueller, F. M. Effect of lattice strain and defects on the superconductivity of MgB_2. *Appl. Phys. Lett.* **2001**, *79*, 4399–4401.

(38) Chen, X. H.; Wang, Y. S.; Xue, Y. Y.; Meng, R. L.; Wang, Y. Q.; Chu, C. W. Correlation between the residual resistance ratio and magnetoresistance in MgB_2. *Phys. Rev. B* **2001**, *65*, 024502.

(39) Zhao, Y. G.; Zhang, X. P.; Qiao, P. T.; Zhang, H. T.; Jia, S. L.; Cao, B. S.; Zhu, M. H.; Han, Z. H.; Wang, X. L.; Gu, B. L. Influence of the starting composition $Mg_{1-x}B_2$ on the structural and superconducting properties of the MgB_2 phase. *Physica C* **2001**, *366*, 1–5.

(40) Mori, H.; Lee, S.; Yamamoto, A.; Tajima, S.; Sato, S. Electron density distribution in a single crystal of $Mg_{1-x}B_2$ [$x = 0.045(5)$]. *Phys. Rev. B* **2002**, *65*, 092507.

(41) Lee, S.; Masui, T.; Mori, H.; Eltsev, Y.; Yamamoto, A.; Tajima, S. Crystal growth and characterization of MgB_2: the relation between structural and superconducting properties. *Supercond. Sci. Technol.* **2003**, *16*, 213–220.

(42) Chen, S. K.; Serquis, A.; Serrano, G.; Yates, K. A.; Blamire, M. G.; Guthrie, D.; Cooper, J.; Wang, H.; Margadonna, S.; MacManus-Driscoll, J. L. Structural and Superconducting Property Variations with Nominal Mg Non-Stoichiometry in Mg_xB_2 and Its Enhancement of Upper Critical Field. *Adv. Funct. Mater.* **2008**, *18*, 113–120.

(43) Zhigadlo, N. D.; Katrych, S.; Karpinski, J.; Batlogg, B.; Bernardini, F.; Massidda, S.; Puzniak, R. Influence of Mg deficiency on crystal structure and superconducting properties in MgB_2 single crystals. *Phys. Rev. B* **2010**, *81*, 054520.

(44) Hinks, D. G.; Jorgensen, J. D.; Zheng, H.; Short, S. Synthesis and stoichiometry of MgB_2. *Physica C* **2002**, *382*, 166–176.

(45) Fischer, A.; Tiana, D.; Scherer, W.; Batke, K.; Eickerling, G.; Svendsen, H.; Bindzus, N.; Iversen, B. B. Experimental and theoretical charge density studies at subatomic resolution. *J. Phys. Chem. A* **2011**, *115*, 13061–13071.

(46) Batke, K.; Eickerling, G. Topology of the Electron Density of d^0 Transition Metal Compounds at Subatomic Resolution. *J. Phys. Chem. A* **2013**, *117*, 11566–11579.

(47) Scherer, W.; Fischer, A.; Eickerling, G. *The Chemical Bond*; Wiley-VCH: Weinheim, 2014; Chapter 9, pp 309–344.

(48) Fischer, A.; Eickerling, G.; Scherer, W. The Effects of Chemical Bonding at Subatomic Resolution: A Case Study on α-Boron. *Molecules* **2021**, *26*, 4270.

(49) Fässler, T. F.; Evers, J. *Zintl Phases - Principles and Recent Developments*, 1st ed.; Springer: Heidelberg, 2011; Chapter 1, pp 13–15.

(50) Kortus, J.; Mazin, I. I.; Belashchenko, K. D.; Antropov, V. P.; Boyer, L. L. Superconductivity of metallic boron in MgB_2. *Phys. Rev. Lett.* **2001**, *86*, 4656.

(51) An, J. M.; Pickett, W. E. Superconductivity of MgB_2: covalent bonds driven metallic. *Phys. Rev. Lett.* **2001**, *86*, 4366.

(52) Harima, H. Energy band structures of MgB_2 and related compounds. *Physica C* **2002**, *378-381*, 18–24.

(53) Wu, L.; Zhu, Y.; Vogt, T.; Su, H.; Davenport, J. W. Valence-electron distribution in MgB_2 by accurate diffraction measurements and first-principles calculations. *Phys. Rev. B* **2004**, *69*, 064501.

(54) Merz, M.; Schweiss, P.; Wolf, T.; von Löhneysen, H.; Schuppler, S. Electronic Structure of Single-Crystalline $Mg_xAl_{1-x}B_2$ Probed by X-ray Diffraction Multipole Refinements and Polarization-Dependent X-ray Absorption Spectroscopy. *J. Phys. Soc. Jpn.* **2014**, *83*, 024714.

(55) Bentley, J. J.; Stewart, R. F. Pseudoatoms in diatomic molecules: restricted radial functions. *Acta Crystallographica* **1976**, *32*, 910–914.

(56) Svendsen, H.; Overgaard, J.; Busselez, R.; Arnaud, B.; Rabiller, P.; Kurita, A.; Nishibori, E.; Sakata, M.; Takata, M.; Iversen, B. B. Multipole electron-density modelling of synchrotron powder diffraction data: the case of diamond. *Acta Crystallographica Section A* **2010**, *66*, 458–469.

(57) Bader, R. F. W. *Atoms in Molecules: A Quantum Theory*, 1st ed.; Clarendon Press: Oxford, 1995.

(58) Popelier, P. *Atoms in Molecules: An Introduction*, 1st ed.; Prentice Hall: Harlow, 2000.

(59) Collins, D. M. Electron density images from imperfect data by iterative entropy maximization. *Nature* **1982**, *298*, 49–51.

(60) Coppens, P. *X-ray Charge Densities and Chemical Bonding*; International Union of Crystallography: Chester, Chapter 5.3, pp 115–120.

(61) Liu, A. Y.; Mazin, I. I.; Kortus, J. Beyond Eliashberg Superconductivity in MgB_2: Anharmonicity, Two-Phonon Scattering, and Multiple Gaps. *Phys. Rev. Lett.* **2001**, *87*, 087005.

(62) Yildirim, T.; Gülseren, O.; Lynn, J. W.; Brown, C. M.; Udovic, T. J.; Huang, Q.; Rogado, N.; Regan, K. A.; Hayward, M. A.; Slusky, J. S. et al. Giant Anharmonicity and Nonlinear Electron-Phonon Coupling in MgB_2: A Combined First-Principles Calculation and Neutron Scattering Study. *Phys. Rev. Lett.* **2001**, *87*, 037001.

(63) Shukla, A.; Calandra, M.; d'Astuto, M.; Lazzeri, M.; Mauri, F.; Bellin, C.; Krisch, M.; Karpinski, J.; Kazakov, S. M.; Jun, J. et al. Phonon Dispersion and Lifetimes in MgB_2. *Phys. Rev. Lett.* **2003**, *90*, 095506.

(64) Baron, A. Q. R.; Uchiyama, H.; Tsutsui, S.; Tanaka, Y.; Ishikawa, D.; Sutter, J. P.; Lee, S.; Tajima, S.; Heid, R.; Bohnen, K.-P. Phonon spectra in pure and carbon doped MgB_2 by inelastic X-ray scattering. *Physica C* **2007**, *456*, 83–91.

(65) Blumberg, G.; Mialitsin, A.; Dennis, B. S.; Zhigadlo, N. D.; Karpinski, J. Multi-gap superconductivity in MgB_2: Magneto-Raman spectroscopy. *Physica C* **2007**, *456*, 75–82.

(66) Calandra, M.; Lazzeri, M.; Mauri, F. Anharmonic and non-adiabatic effects in MgB_2: Implications for the isotope effect and interpretation of Raman spectra. *Physica C* **2007**, *456*, 38–44.

(67) d'Astuto, M.; Calandra, M.; Reich, S.; Shukla, A.; Lazzeri, M.; Mauri, F.; Karpinski, J.; Zhigadlo, N. D.; Bossak, A.; Krisch, M. Weak anharmonic effects in MgB_2: A comparative inelastic x-ray scattering and Raman study. *Phys. Rev. B* **2007**, *75*, 174508.

(68) Mialitsin, A.; Dennis, B. S.; Zhigadlo, N. D.; Karpinski, J.; Blumberg, G. Anharmonicity and self-energy effects of the E_{2g} phonon in MgB_2. *Phys. Rev. B* **2007**, *75*, 020509.

(69) Stewart, R. F. V. One-Electron Density Functions and Many-Centered Finite Multipole Expansions. *Isr. J. Chem.* **1977**, *16*, 124–131.

(70) Harris, C. R.; Millman, K. J.; van der Walt, S. J.; Gommers, R.; Virtanen, P.; Cournapeau, D.; Wieser, E.; Taylor, J.; Berg, S.; Smith, N. J. et al. Array programming with NumPy. *Nature* **2020**, *585*, 357–362.

(71) Dovesi, R.; Saunders, V. R.; Roetti, C.; Orlando, R.; Zicovich-Wilson, C. M.; Pascale, F.; Civalleri, B.; Doll, K.; Harrison, N. M.; Bush, I. J. et al. CRYSTAL17 Users's Manual. 2017.

(72) Dovesi, R.; Erba, A.; Orlando, R.; Zicovich-Wilson, C. M.; Civalleri, B.; Maschio, L.; Rérat, M.; Casassa, S.; Baima, J.; Salustro, S. et al. Quantum-mechanical condensed matter simulations with CRYSTAL. *Comput. Mol. Sci.* **2018**, *8*, e1360.

(73) Otero-de-la Roza, A.; Blanco, M. A.; Pendás, A. M.; Luaña, V. Critic: a new program for the topological analysis of solid-state electron densities. *Comput. Phys. Commun.* **2009**, *180*, 157 – 166.

(74) Otero-de-la Roza, A.; Johnson, E. R.; Luaña, V. Critic2: A program for real-space analysis of quantum chemical interactions in solids. *Comput. Phys. Commun.* **2014**, *185*, 1007–1018.

(75) Batke, K. Die Topologie der Elektronendichte von Übergangsmetallverbindungen bei Subatomarer Auflösung. Ph.D. thesis, University of Augsburg, 2017.

(76) DIRAC, a relativistic ab initio electronic structure program, Release DIRAC22 (2022), written by H. J. Aa. Jensen, R. Bast, A. S. P. Gomes, T. Saue and L. Visscher, with contributions from I. A. Aucar, V. Bakken, C. Chibueze, J. Creutzberg, K. G. Dyall,

S. Dubillard, U. Ekström, E. Eliav, T. Enevoldsen, E. Faßhauer, T. Fleig, O. Fossgaard, L. Halbert, E. D. Hedegård, T. Helgaker, B. Helmich–Paris, J. Henriksson, M. van Horn, M. Iliaš, Ch. R. Jacob, S. Knecht, S. Komorovský, O. Kullie, J. K. Lærdahl, C. V. Larsen, Y. S. Lee, N. H. List, H. S. Nataraj, M. K. Nayak, P. Norman, G. Olejniczak, J. Olsen, J. M. H. Olsen, A. Papadopoulos, Y. C. Park, J. K. Pedersen, M. Pernpointner, J. V. Pototschnig, R. di Remigio, M. Repisky, K. Ruud, P. Sałek, B. Schimmelpfennig, B. Senjean, A. Shee, J. Sikkema, A. Sunaga, A. J. Thorvaldsen, J. Thyssen, J. van Stralen, M. L. Vidal, S. Villaume, O. Visser, T. Winther, S. Yamamoto and X. Yuan (available at `http://dx.doi.org/10.5281/zenodo.6010450`, see also `http://www.diracprogram.org`).

(77) The Elk Code. `http://elk.sourceforge.net/`.

Graphical TOC Entry

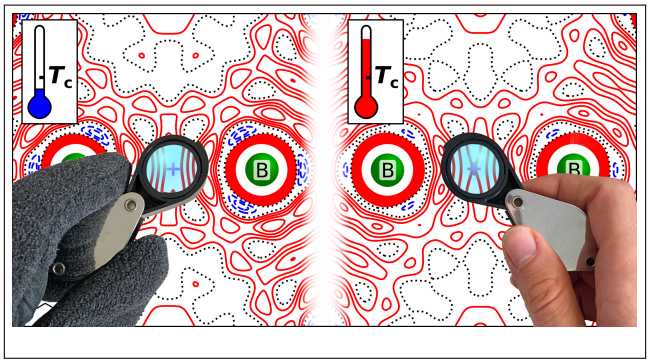

Supporting Information: X-ray charge-density studies – a suitable probe for superconductivity?

Jan Langmann,[†] Hasan Kepenci,[†] Georg Eickerling,[*,†] Kilian Batke,[†] Anton Jesche,[‡] Mingyu Xu,[¶,§] Paul Canfield,[¶,§] and Wolfgang Scherer[*,†]

†*CPM, Institut für Physik, Universität Augsburg, 86159 Augsburg, Germany*

‡*Experimentalphysik VI, Zentrum für Elektronische Korrelation und Magnetismus, Institut für Physik, Universität Augsburg, 86159 Augsburg, Germany*

¶*The Ames Laboratory, Iowa State University, Ames, Iowa 50011, USA*

§*Department of Physics and Astronomy, Iowa State University, Ames, IA 50011, USA*

E-mail: georg.eickerling@uni-a.de; wolfgang.scherer@uni-a.de

Phone: +49 (0)821 598 3362; +49 (0)821 598 3350

Crystal growth

Single crystals of MgB_2 were grown by a high pressure method from excess solution of magnesium. Elemental Mg and B were packed inside a 1 cm diameter boron nitride (BN) crucible in the ratio of Mg:B = 1:0.7. A pressed Mg-pellet and B powder were placed in the crucible and the crucible was tightly packed with BN powder to prevent any Mg leakage at high pressure and temperature. Using a cubic anvil furnace, a pressure of 3.5 GPa was applied to the crucible at room temperature, and it was then heated to 1430 °C and held at this temperature for 1 hr. Afterwards the temperature was decreased to the 650 °C melting point of Mg over a time of 6 hrs. After completion of the crystal growth, the furnace heating was turned off to achieve a faster cooling and then the pressure was released. This procedure yields MgB_2 single crystals embedded inside the solidified Mg-melt. Individual single crystals were extracted by distilling the excess Mg at 750 °C inside an evacuated quartz tube. Given that the heater used in the high temperature/high pressure furnace is a graphite tube, a slight C-doping is possible, reducing T_c slightly from the reported value for pure MgB_2.

Investigated samples

Crystal 1

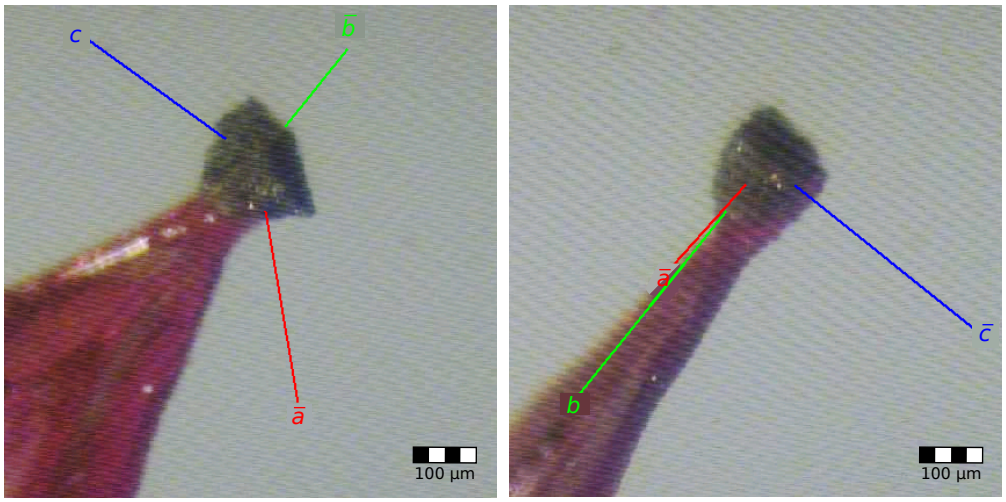

Figure S1: Photographic image of MgB_2 single crystal 1 used in the XRD experiments. Crystal axes a, b and c referring to the hexagonal unit cell are indicated by colored lines.

Crystal 2

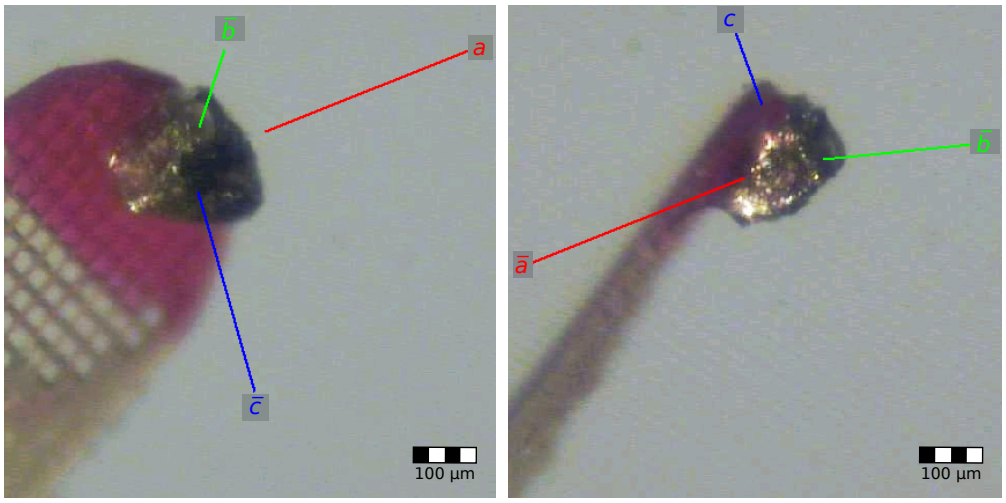

Figure S2: Photographic image of MgB_2 single crystal 2 used in the magnetization measurements. Crystal axes a, b and c referring to the hexagonal unit cell are indicated by colored lines.

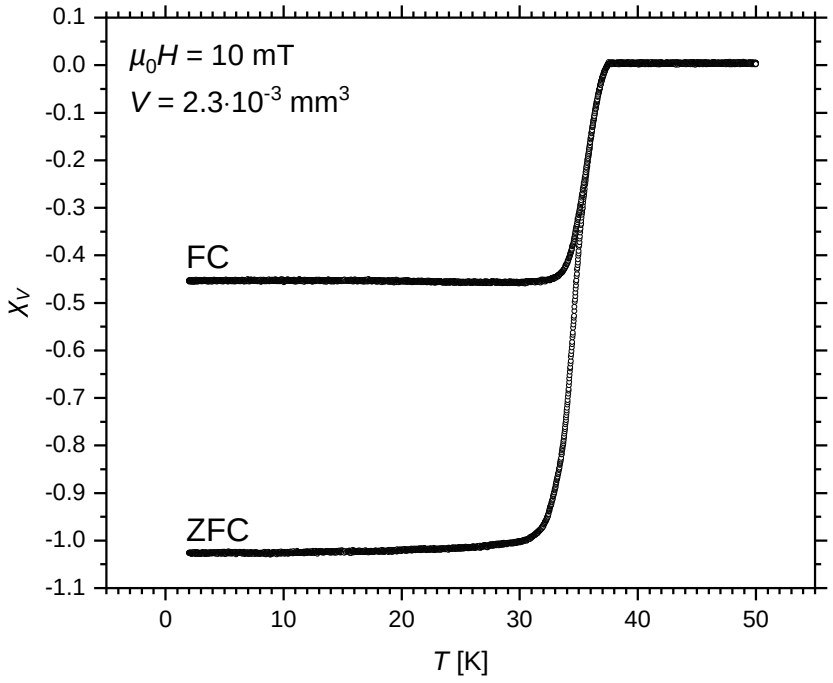

Figure S3: Temperature-dependent DC magnetization of crystal 2 measured under zero-field cooling (ZFC) and field-cooling (FC) conditions in an applied field $\mu_0 H = 10$ mT.

Single-crystal XRD experiments

Overview

experiment	**1**	**2**
sample	crystal 1	crystal 1
sample dim. [µm^3]	132×138×180	132×138×180
sample photo	Fig. S1	Fig. S1
diffractometer	1	2
temperature(s) [K]	100(2)	13.5(5) 25.086(5) 45.009(7) 298.3(1)
sample cooling	open-flow N_2	closed-cycle He
vacuum chamber	–	beryllium domes

Table S1: Overview of the single-crystal XRD experiments on MgB_2. The numbering of diffractometer setups is explained in the Methods Section of the main paper.

Details

experiment number in Tab. S1	1
temperature	100(2) K
unit cell dimensions	$a = 3.0849(1)$ Å
	$c = 3.5113(2)$ Å
	$V = 28.939(3)$ Å^3
calculated density	2.6213 g·cm^{-3}
sample	crystal 1
crystal size	132×138×180 µm^3
wave length	0.56087 Å
absorption correction	multi-scan
transm. ratio (max/min)	0.9582 / 0.9283
absorption coefficient	0.322 mm^{-1}
$F(000)$	22
θ range	5° to 63°
range in hkl	-9/9, -9/8, -11/10
total no. reflections	15642
independent reflections	237 ($R_{\text{int}} = 0.0245$)
reflections with $I \geq 3\sigma(I)$	237

Table S2: Experimental parameters of the high-resolution single-crystal XRD data set collected for crystal 1 at a temperature of 100(2) K (experiment 1 in Tab. S1).

T [K]	298.3(1)	45.009(7)
experiment number in Tab. S1	2	2
unit cell dimensions	$a = 3.09413(12)$ Å $c = 3.52625(15)$ Å $V = 29.236(2)$ Å^3	$a = 3.08861(4)$ Å $c = 3.51561(6)$ Å $V = 29.044(1)$ Å^3
calculated density	2.6085 g·cm^{-3}	2.6257 g·cm^{-3}
crystal size	132×138×180 µm^3	
wave length	0.56087 Å	
absorption correction	multi-scan	
transm. ratio (max/min)	0.9824 / 0.9354	0.9825 / 0.9323
absorption coefficient	0.321 mm^{-1}	0.323 mm^{-1}
$F(000)$	22	
θ range	5° to 48°	
range in hkl	-4/7, -8/4, -9/9	-4/7, -8/4, -9/9
total no. reflections	3387	3389
independent reflections	148 ($R_{\text{int}} = 0.004$)	148 ($R_{\text{int}} = 0.004$)
reflections with $I \geq 3\sigma(I)$	148	148

Table S3: Experimental parameters of the low-temperature XRD data sets collected for crystal 1 at temperatures of 298.3(1) K and 45.009(7) K (experiment 2 in Tab. S1).

T [K]	25.086(5) K	13.5(5) K
experiment number in Tab. S1	2	2
unit cell dimensions	$a = 3.08836(3)$ Å	$a = 3.08934(3)$ Å
	$c = 3.51515(6)$ Å	$c = 3.51629(5)$ Å
	$V = 29.036(1)$ Å^3	$V = 29.063(1)$ Å^3
calculated density	2.6263 g·cm^{-3}	2.6240 g·cm^{-3}
crystal size	132×138×180 µm^3	
wave length	0.56087 Å	
absorption correction	multi-scan	
transm. ratio (max/min)	0.9824 / 0.9310	0.9824 / 0.9421
absorption coefficient	0.323 mm^{-1}	0.323 mm^{-1}
$F(000)$	22	
θ range	5° to 48°	
range in hkl	-4/7, -8/4, -9/9	-4/8, -8/4, -9/9
total no. reflections	3387	3387
independent reflections	148 ($R_{\text{int}} = 0.0038$)	148 ($R_{\text{int}} = 0.0036$)
reflections with $I \geq 3\sigma(I)$	148	148

Table S4: Experimental parameters of the low-temperature XRD data sets collected for crystal 1 at temperatures of 25.086(5) K and 13.5(5) K (experiment 2 in Tab. S1).

Comparability of temperature-dependent XRD experiments

Several measures were taken to ensure comparability between single-crystal XRD data sets collected at different temperatures (experiment 2 in Tab. S1; data set parameters in Tab. S3):

1. All temperature-dependent measurements on a sample were taken in direct sequence without re-orientation and without interruption of cooling.

2. Integration and reduction of all data sets were performed with identical parameters in EVAL14[S1] and SADABS,[S2] respectively.

3. Only reflections which have been collected at all four temperature points were read into SADABS[S2] for data reduction to limit the data sets to the same number of hkl reflections. Intensities of symmetry-equivalent reflections were merged.

Resolution dependence of the magnesium site occupation factor

IAM using static theoretical structure factors

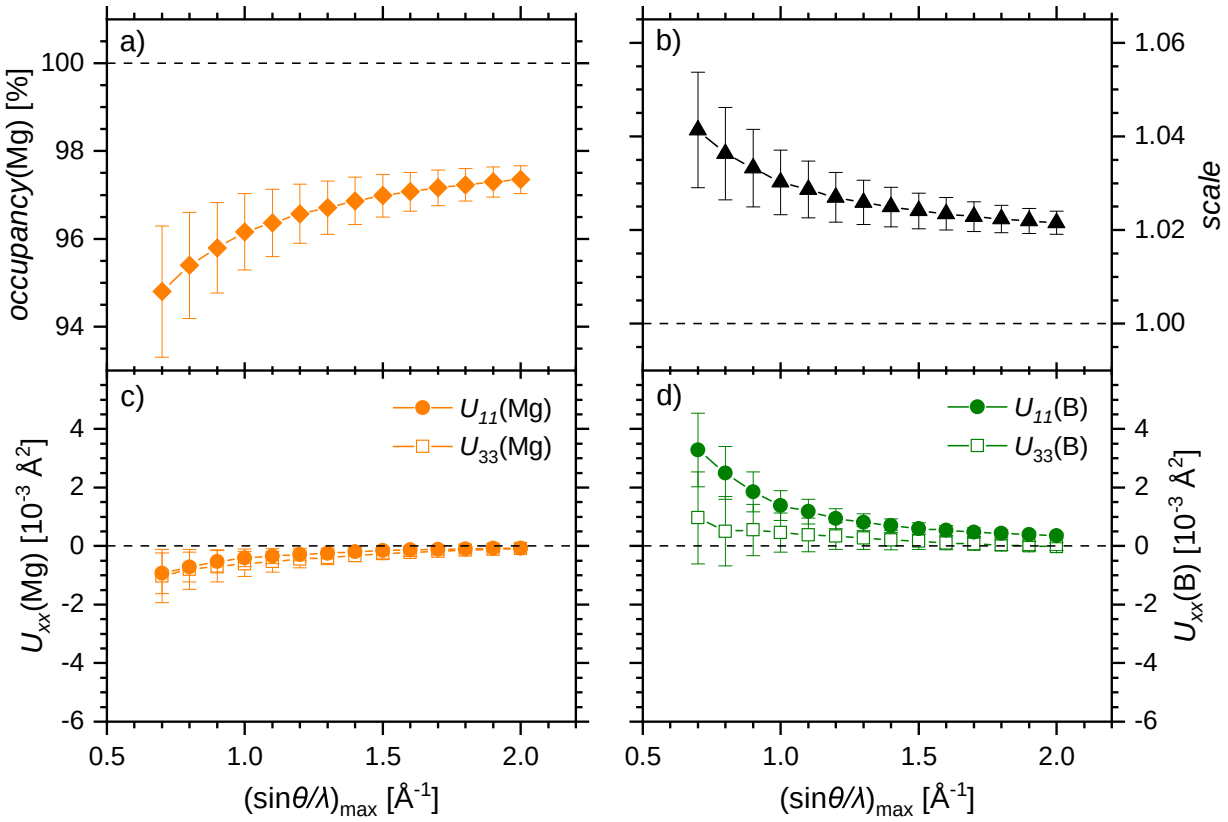

Figure S4: Variation of a) the magnesium site occupancy, b) the scale factor, and the anisotropic ADPs U_{11} and U_{33} for c) the magnesium atom and d) the boron atom with increasing resolution $(\sin\theta/\lambda)_{max}$ of static theoretical structure factors. All given parameters were refined simultaneously employing IAMs based on scattering factors for neutral atoms. Expected parameter values are marked by dashed horizontal lines, while error bars denote the estimated standard deviation $(1 \times \sigma)$ of the parameter values as obtained from least-squares refinement using unit weights for all reflection intensities.

IAM using experimental XRD data

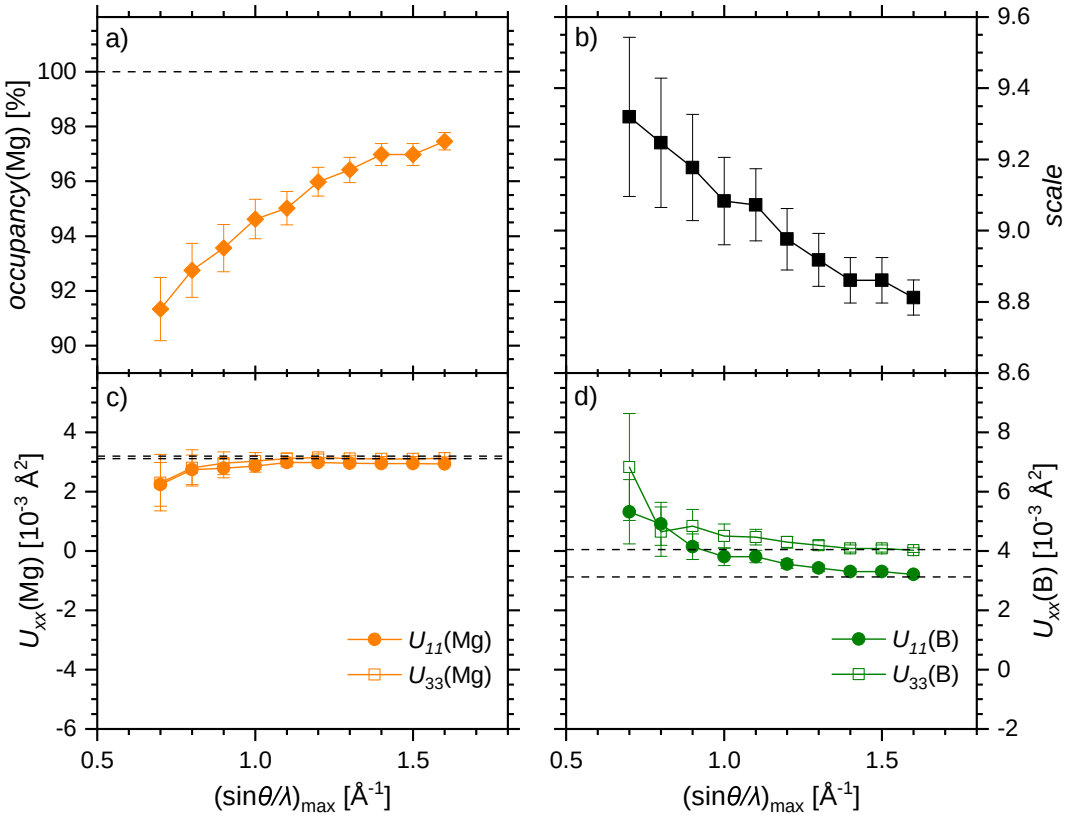

Figure S5: Variation of a) the magnesium site occupation factor, b) the scale factor, and the anisotropic ADPs U_{11} and U_{33} for c) the magnesium atom and d) the boron atom with increasing resolution $(\sin\theta/\lambda)_{max}$ of experimental single-crystal XRD data (experiment 1 in Tab. S1; data set parameters in Tab. S2). All given parameters were refined simultaneously employing IAMs based on scattering factors for neutral atoms. Expected parameter values are marked by dashed horizontal lines. In case of c) and d) these are the ADP values for $T = 100$ K derived from DFT calculations. Error bars refer to the estimated standard deviation $(1 \times \sigma)$ of the parameter values as obtained from least-squares refinement.

EHC multipolar model using static theoretical structure factors

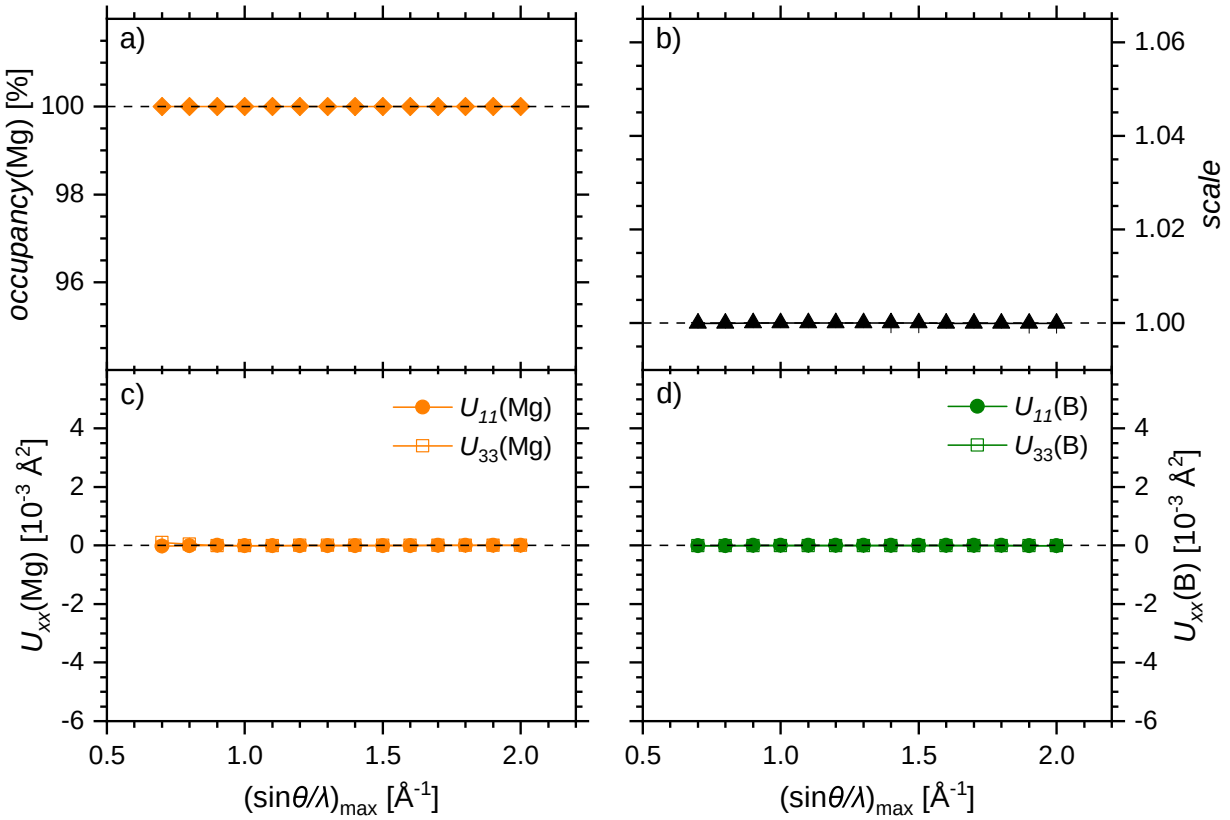

Figure S6: Variation of a) the magnesium site occupancy, b) the scale factor, and the anisotropic ADPs U_{11} and U_{33} for c) the magnesium atom and d) the boron atom with increasing resolution $(\sin\theta/\lambda)_{max}$ of static theoretical structure factors. All given parameters were refined simultaneously employing EHC models with multipolar parameters fixed to their values in T-EHCM1 (Tab. S5). Expected parameter values are marked by dashed horizontal lines, while error bars denote the estimated standard deviation $(1\times\sigma)$ of the parameter values as obtained from least-squares refinement using unit weights for all reflection intensities.

EHC multipolar model using experimental XRD data

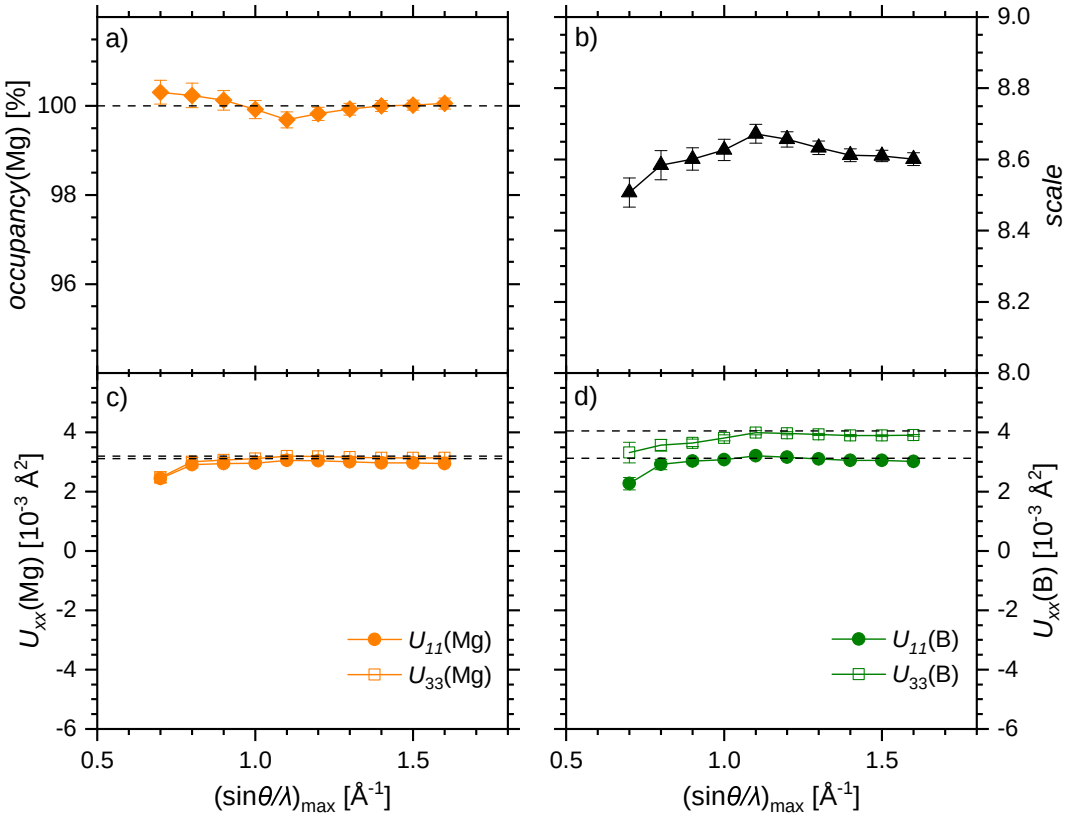

Figure S7: Variation of a) the magnesium site occupation factor, b) the scale factor, and the anisotropic ADPs U_{11} and U_{33} for c) the magnesium atom and d) the boron atom with increasing resolution $(\sin\theta/\lambda)_{max}$ of experimental single-crystal XRD data (experiment 1 in Tab. S1; data set parameters in Tab. S2). All given parameters were refined simultaneously employing EHC models with multipolar parameters fixed to their values in E-EHCM1 (Tab. S6). Expected parameter values are marked by dashed horizontal lines. In case of c) and d) this is the ADP values for $T = 100$ K derived from DFT calculations. Error bars refer to the estimated standard deviation $(1 \times \sigma)$ of the parameter values as obtained from least-squares refinement.

Multipolar models

Local coordinate systems

All multipolar models in this paper refer to the same local coordinate systems for the two symmetry-independent atoms in the MgB_2 structure, *i.e.* Mg and B. In both cases, the local x and z axes are oriented parallel to the a and c axes of the unit cell, respectively. The y axes are chosen to complete the right-handed orthonormal coordinate systems.

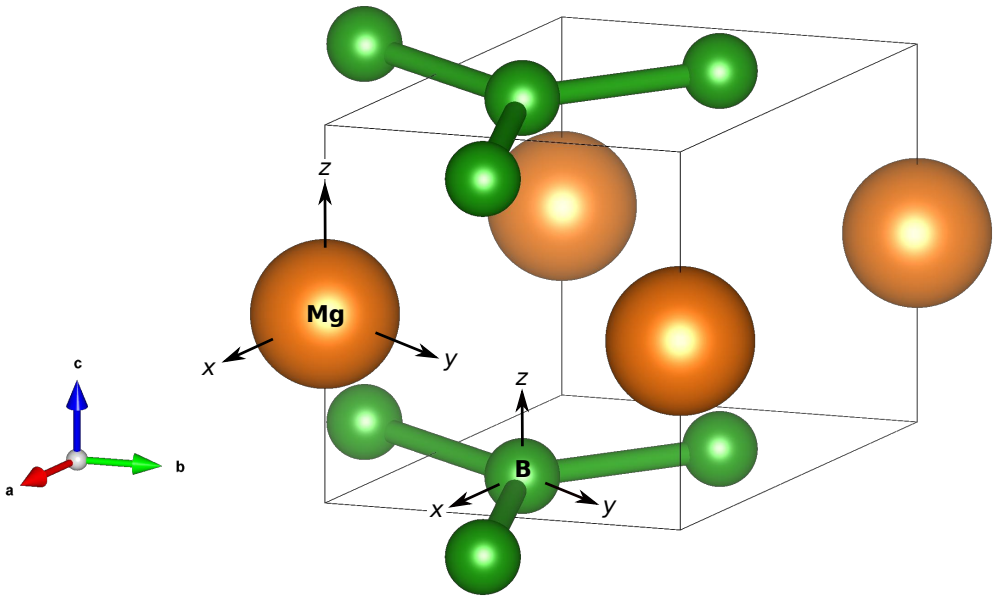

Figure S8: Definition of local coordinate systems for the two symmetry-independent atoms Mg and B.

Model parameters

EHC models using static theoretical structure factors

		T-EHCM1		T-EHCM2
	scale	1.0*		1.01007(19)
Mg1	*occ.*	1.0*		1.00152(14)
[ ]($1s^2$)	x		0*	
	y		0*	
	z		0.5*	
	U_{11} [Å^2]	0.0*		0.000078(4)
	U_{33} [Å^2]	0.0*		0.000081(4)
	P_c		0.0*	
	P_v	1.9781(7)		1.9671(7)
	κ	1.0148(7)		1.0363(12)
Mg2	*occ.*	1.0*		1.00152*
[ ]($2s^2$, $2p^6$)	x		0*	
	y		0*	
	z		0.5*	
	U_{11} [Å^2]	0.0*		0.000078*
	U_{33} [Å^2]	0.0*		0.000081*
	P_c		0.0*	
	P_v	7.968863*		7.916841*
	κ	1.01006(9)		1.01055(10)

		T-EHCM1		**T-EHCM2**
Mg3	*occ.*	1.0*		1.00152*
[ ]($3s^2$)	x		0*	
	y		0*	
	z		0.5*	
	U_{11} [Å^2]	0.0*		0.000078*
	U_{33} [Å^2]	0.0*		0.000081*
	P_c		0.0*	
	P_v	1.9142(4)		1.9399(15)
	κ	0.7939(17)		0.7981(16)
	κ'	1.363(7)		1.366(6)
	P_{20}	0.0025(6)		0.0016(6)
	P_{40}	-0.1556(17)		-0.1555(17)
B1	*occ.*	1.0*		1.0*
[ ]($1s^2$)	x		$\frac{2}{3}$*	
	y		$\frac{1}{3}$*	
	z		0*	
	U_{11} [Å^2]	0.0*		-0.000085(5)
	U_{33} [Å^2]	0.0*		-0.000091(5)
	P_c		0.0*	
	P_v	1.9777(4)		1.9860(4)
	κ	1.00554(19)		0.9922(4)

		T-EHCM1		**T-EHCM2**
B2	*occ.*	1.0*		1.0*
[ ]($2s^1$)	x		$\frac{2}{3}$*	
	y		$\frac{1}{3}$*	
	z		0*	
	U_{11} [Å^2]	0.0*		-0.000085*
	U_{33} [Å^2]	0.0*		-0.000091*
	P_c		0.0*	
	P_v	1.5874(7)		1.5888(7)
	κ	0.9161(9)		0.9468(8)
	κ'	0.9586(18)		0.9562(18)
	P_{20}	-0.0727(3)		-0.0727(3)
	P_{33-}	0.0816(4)		0.0816(4)
	P_{40}	0.0019(3)		0.0019(3)

		T-EHCM1	**T-EHCM2**
B3	*occ.*	1.0*	1.0*
[ ](2p^2)	x	$\frac{2}{3}$*	
	y	$\frac{1}{3}$*	
	z	0*	
	U_{11} [Å^2]	0.0*	-0.000085*
	U_{33} [Å^2]	0.0*	-0.000091*
	P_c	0.0*	
	P_v	1.5044(8)	1.5133(8)
	κ	1.0744(13)	1.0040(14)
	κ'	0.9586*	0.9562*
	P_{20}	-0.0727*	-0.0727*
	P_{33-}	0.0816*	0.0816*
	P_{40}	0.0019*	0.0019*
independent reflections		238	
data / parameters		13.22	9.92
goodness-of-fit on F^2		0.01	0.01
R (all data)		0.03	0.02
wR (all data)		0.03	0.03
largest diff. peak and hole [e·Å^{-3}]		0.02/-0.02	0.01/-0.01

Table S5: Model parameters refined using static theoretical structure factors up to a resolution of $(\sin\theta/\lambda)_{max} = 1.6$ Å^{-1}. Parameter values marked by an asterisk ($*$) were not refined or subject to constraints. In T-EHCM1 scale factor, thermal parameters U_{11} and U_{33} for Mg and B, and the occupation factor for Mg were fixed. In T-EHCM2, these parameters were refined simultaneously with the multipolar parameters.

EHC models using experimental XRD data

		E-EHCM1	**E-EHCM2**
	scale	74.1(2)	71.9(5)
Mg1	*occ.*	1.0*	1.015(3)
[ ]($1s^2$)	x	0*	
	y	0*	
	z	0.5*	
	U_{11} [Å^2]	0.002950(14)	0.002947(14)
	U_{33} [Å^2]	0.003143(17)	0.003140(17)
	P_c	0.0*	
	P_v	1.978130*	
	κ	1.014839*	
Mg2	*occ.*	1.0*	1.015*
[ ]($2s^2$, $2p^6$)	x	0*	
	y	0*	
	z	0.5*	
	U_{11} [Å^2]	0.002950*	0.002947*
	U_{33} [Å^2]	0.003143*	0.003140*
	P_c	0.0*	
	P_v	7.968863*	
	κ	1.010059*	

		E-EHCM1	**E-EHCM2**
Mg3	*occ.*	1.0*	1.015*
[ ]($3s^2$)	x	0*	
	y	0*	
	z	0.5*	
	U_{11} [Å^2]	0.002950*	0.002947*
	U_{33} [Å^2]	0.003143*	0.003140*
	P_c	0.0*	
	P_v	1.6(3)	1.5(3)
	κ	0.81(8)	0.82(8)
	κ'	1.362923*	
	P_{20}	-0.04(5)	-0.04(5)
	P_{40}	-0.46(11)	-0.42(11)
B1	*occ.*	1.0*	1.0*
[ ]($1s^2$)	x	$\frac{2}{3}$*	
	y	$\frac{1}{3}$*	
	z	0*	
	U_{11} [Å^2]	0.00303(3)	0.00298(3)
	U_{33} [Å^2]	0.00391(4)	0.00387(4)
	P_c	0.0*	
	P_v	1.977650*	
	κ	1.005537*	

		E-EHCM1		**E-EHCM2**
B2	*occ.*	1.0*		1.0*
[ ]($2s^1$)	x		$\frac{2}{3}$*	
	y		$\frac{1}{3}$*	
	z		0*	
	U_{11} [Å^2]	0.00303*		0.00298*
	U_{33} [Å^2]	0.00391*		0.00387*
	P_c		0.0*	
	P_v	1.60(12)		2.330861*
	κ	0.90(2)		0.852(16)
	κ'	1.11(11)		1.16(11)
	P_{20}	-0.063(18)		-0.058(16)
	P_{33-}	0.051(16)		0.046(15)
	P_{40}	-0.007(13)		-0.002(11)

		E-EHCM1	**E-EHCM2**
B3	*occ.*	1.0*	1.0*
[ ](2p^2)	x	$\frac{2}{3}$*	
	y	$\frac{1}{3}$*	
	z	0*	
	U_{11} [Å^2]	0.00303*	0.00298*
	U_{33} [Å^2]	0.00391*	0.00387*
	P_c	0.0*	
	P_v	1.665498*	0.97(17)
	κ	0.98(5)	1.24(9)
	κ'	1.11*	1.16*
	P_{20}	-0.063*	-0.058*
	P_{33-}	0.051*	0.046*
	P_{40}	-0.007*	-0.002*
independent reflections		237	
data / parameters		14.81	13.94
goodness-of-fit on F^2		0.92	0.91
R (all data)		0.69	0.69
wR (all data)		1.96	1.95
largest diff. peak and hole [e·Å^{-3}]		0.2/-0.22	0.2/-0.22

Table S6: Model parameters refined using experimental x-ray diffraction data (resolution $(\sin\theta/\lambda)_{max} = 1.6$ Å^{-1}; experiment 1 in Tab. S1; data set parameters in Tab. S2) collected at $T = 100(2)$ K. Parameter values marked by an asterisk ($*$) were not refined or subject to constraints. In E-EHCM1 the occupation factor for Mg was fixed, while it was refined in E-EHCM2.

SHC models using temperature-dependent experimental XRD data

		298.3 K	**45.009 K**
	scale	8.72(4)	8.56(4)
Mg	*occ.*	1.0*	
$[1s^2](2s^2, 2p^6)$	x	0*	
	y	0*	
	z	0.5*	
	U_{11} [Å^2]	0.00543(6)	0.00299(5)
	U_{33} [Å^2]	0.00585(7)	0.00309(5)
	P_c	2.0*	
	P_v	8.028831*	8.054975*
	κ	1.004(4)	1.011(2)
	κ'	1.0*	
	P_{20}	0.023(14)	0.020(9)

		298.3 K	**45.009 K**
B	*occ.*	1.0*	
$[1s^2](2s^1, 2p^2)$	x	$\frac{2}{3}$*	
	y	$\frac{1}{3}$*	
	z	0*	
	U_{11} [Å^2]	0.00422(8)	0.00303(6)
	U_{33} [Å^2]	0.00577(9)	0.00372(7)
	P_c	2.0*	
	P_v	3.99(3)	3.97(3)
	κ	0.82(3)	0.83(3)
	κ'	0.76(9)	0.74(8)
	P_{20}	-0.22(9)	-0.21(9)
	P_{33-}	0.39(12)	0.41(11)
independent reflections		148	148
data / parameters		12.33	12.33
goodness-of-fit on F^2		1.74	1.18
R (all data)		0.95	0.65
wR (all data)		3.78	2.41
largest diff. peak and hole [e·Å^{-3}]		0.44/-0.33	0.13/-0.23

Table S7: Model parameters refined using experimental XRD data ($(\sin\theta/\lambda)_{max} = 1.3$ Å^{-1}; experiment 2 in Tab. S1; data set parameters in Tab. S3) collected at temperatures of 298.3 K and 45.009 K. Parameter values marked by an asterisk (∗) were not refined or subject to constraints.

		25.086 K	**13.5 K**
	scale	26.90(9)	27.07(12)
Mg	*occ.*	1.0*	
$[1s^2](2s^2,\ 2p^6)$	x	0*	
	y	0*	
	z	0.5*	
	U_{11} [Å^2]	0.00292(4)	0.00301(5)
	U_{33} [Å^2]	0.00305(4)	0.00313(6)
	P_c	2.0*	
	P_v	8.098066*	8.029143*
	κ	1.008(2)	1.010(3)
	κ'	1.0*	
	P_{20}	0.009(9)	0.00(1)

		25.086 K		**13.5 K**
B	*occ.*		1.0*	
$[1s^2](2s^1, 2p^2)$	x		$\frac{2}{3}$*	
	y		$\frac{1}{3}$*	
	z		0*	
	U_{11} [Å^2]	0.00300(4)		0.00304(6)
	U_{33} [Å^2]	0.00362(5)		0.00375(7)
	P_c		2.0*	
	P_v	3.95(2)		3.99(3)
	κ	0.83(2)		0.83(3)
	κ'	0.76(6)		0.80(9)
	P_{20}	-0.23(6)		-0.20(9)
	P_{33-}	0.41(8)		0.37(10)
independent reflections		148		148
data / parameters		12.33		12.33
goodness-of-fit on F^2		1.15		1.26
R (all data)		0.57		0.69
wR (all data)		2.32		2.56
largest diff. peak and hole [e·Å^{-3}]		0.15/-0.18		0.10/-0.22

Table S8: Model parameters refined using experimental x-ray diffraction data ($(\sin\theta/\lambda)_{max}$ = 1.3 Å^{-1}; experiment 2 in Tab. S1; data set parameters in Tab. S4) collected at temperatures of 25.086 K and 13.5 K. Parameter values marked by an asterisk (∗) were not refined or subject to constraints.

Residual electron density maps

Resolution dependence

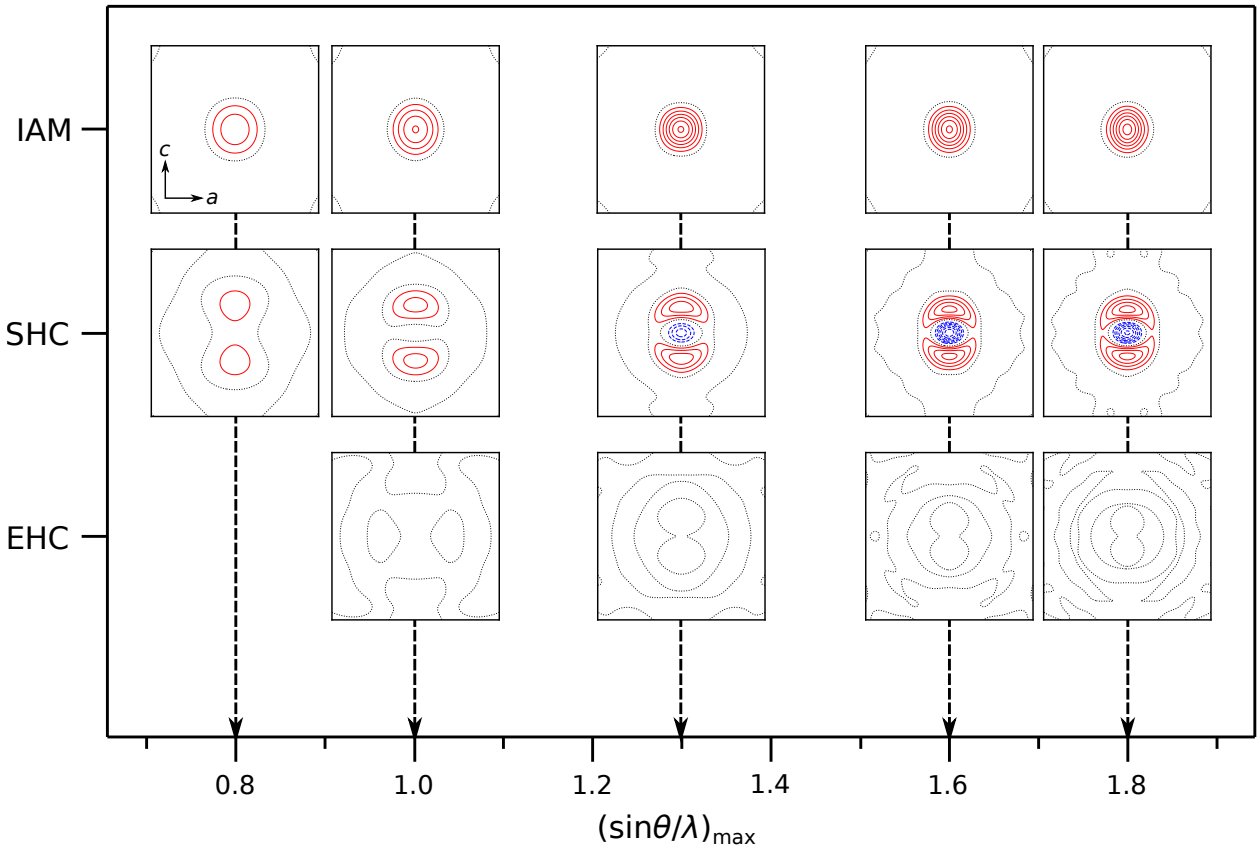

Figure S9: Variation of the residual electron density centered at the magnesium position in the *a*-*c* plane with increasing resolution $(\sin\theta/\lambda)_{\max}$ of static theoretical structure factors for different scenarios: using a) an IAM based on form factors of neutral atoms, b) an SHC model in analogy to Tab. S7 and Tab. S8, or c) and EHC model. In case of b) and c) core and/or valence multipolar parameters were refined at each $(\sin\theta/\lambda)_{\max}$. Iso-contour lines are drawn at ± 0.05 $e{\cdot}\text{Å}^{-3}$ using solid red lines for positive, dotted black lines for zero and dashed blue lines for negative values of the residual electron density, respectively.

EHC models using static theoretical structure factors

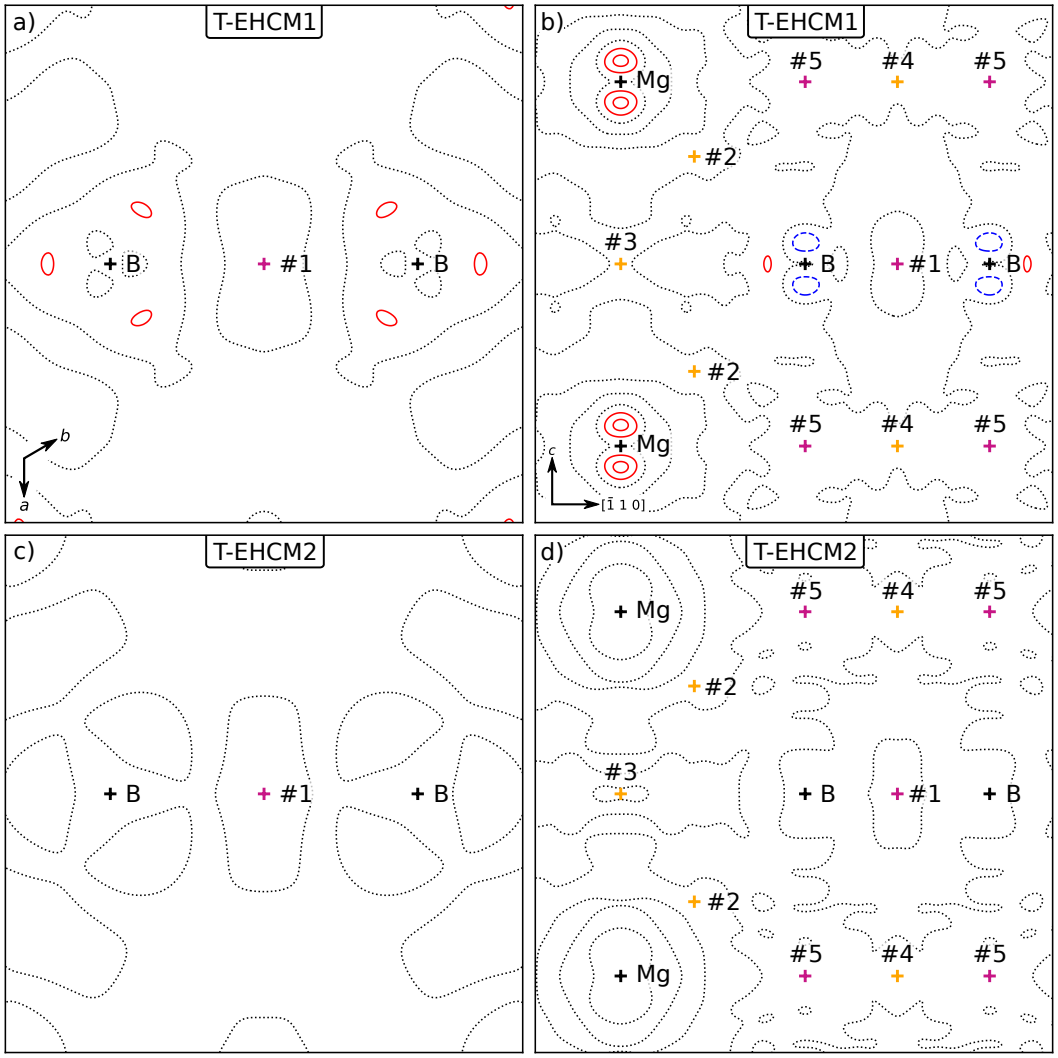

Figure S10: Residual electron density maps for the Extendend Hansen-Coppens (EHC) models T-EHCM1 (a,b) and T-EHCM2 (c,d; Tab. S5) refined using static theoretical structure factors. Maps are oriented parallel (a,c) and perpendicular (b,d) to the hexagonal boron layers in MgB_2. Iso-contour lines are drawn at $\pm\mathbf{0.01}$ $e{\cdot}\text{Å}^{-3}$ using solid red lines for positive, dotted black lines for zero and dashed blue lines for negative values of the residual electron density, respectively.

EHC models using experimental XRD data

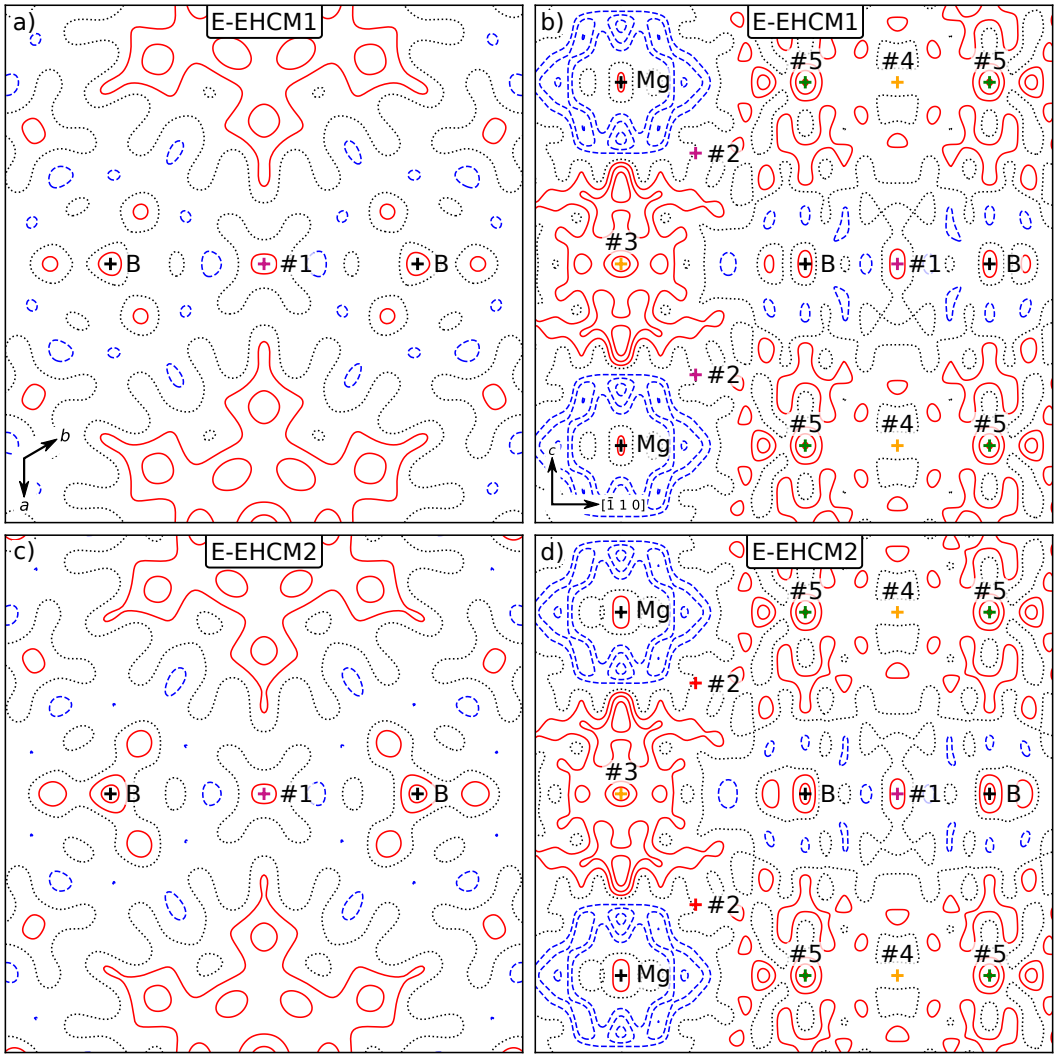

Figure S11: Residual electron density maps for the Extendend Hansen-Coppens (EHC) models E-EHCM1 (a,b) and E-EHCM2 (c,d) (Tab. S6) refined using experimental XRD data ($(\sin\theta/\lambda)_{max}$ = 1.6 Å^{-1}; experiment 1 in Tab. S1; data set parameters in Tab. S2) collected at T = 100(2) K. Maps are oriented parallel (a,c) and perpendicular (b,d) to the hexagonal boron layers in MgB_2. Iso-contour lines are drawn at ±0.05 e·Å^{-3} using solid red lines for positive, dotted black lines for zero and dashed blue lines for negative values of the residual electron density, respectively.

SHC models using temperature-dependent experimental XRD data

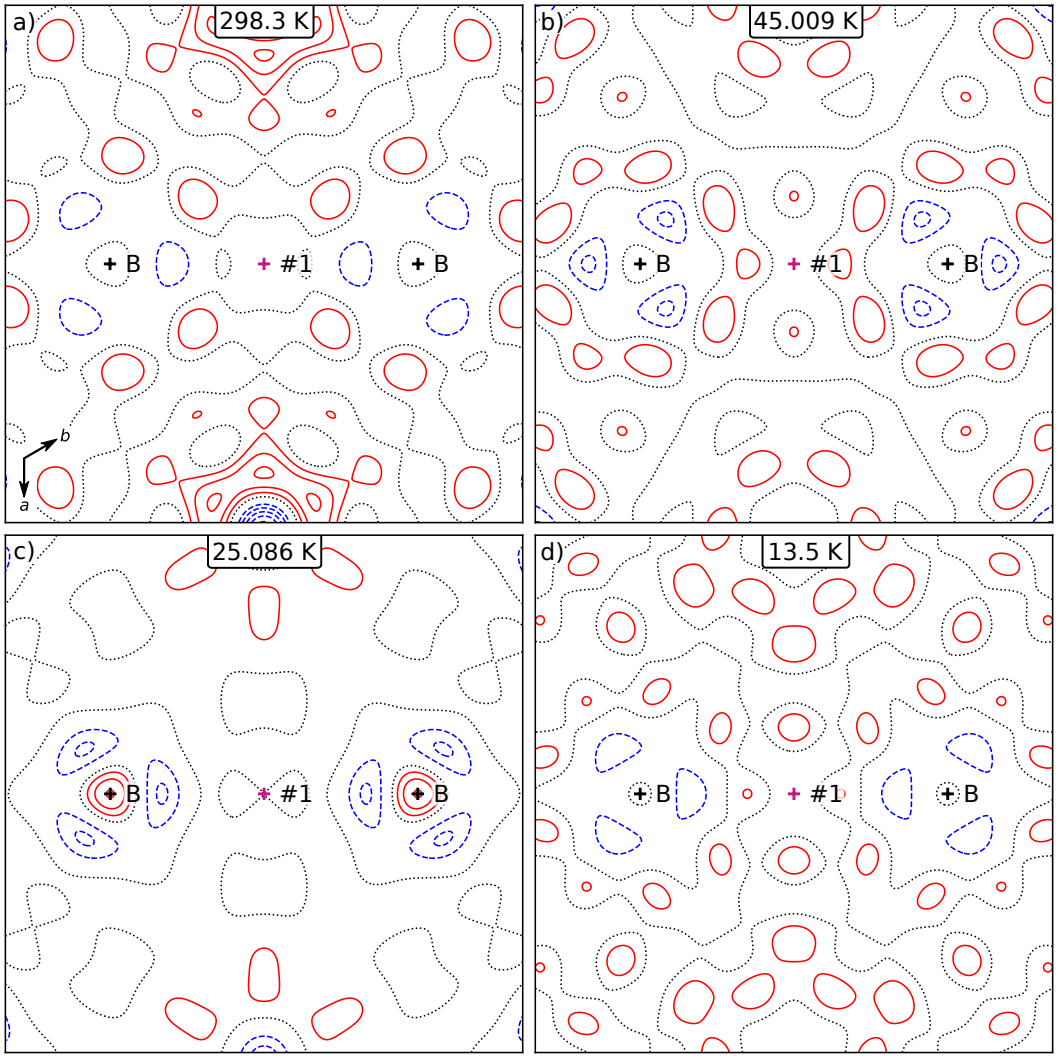

Figure S12: Residual electron density maps for SHC multipolar models refined using experimental XRD data collected at temperatures between a) 298.3(1) K and d) 13.5(5) K (Tab. S7 and Tab. S8). Maps are oriented parallel to the hexagonal boron layers in MgB_2. Iso-contour lines are drawn at ± 0.05 $e{\cdot}\text{Å}^{-3}$ using solid red lines for positive, dotted black lines for zero and dashed blue lines for negative values of the residual electron density, respectively.

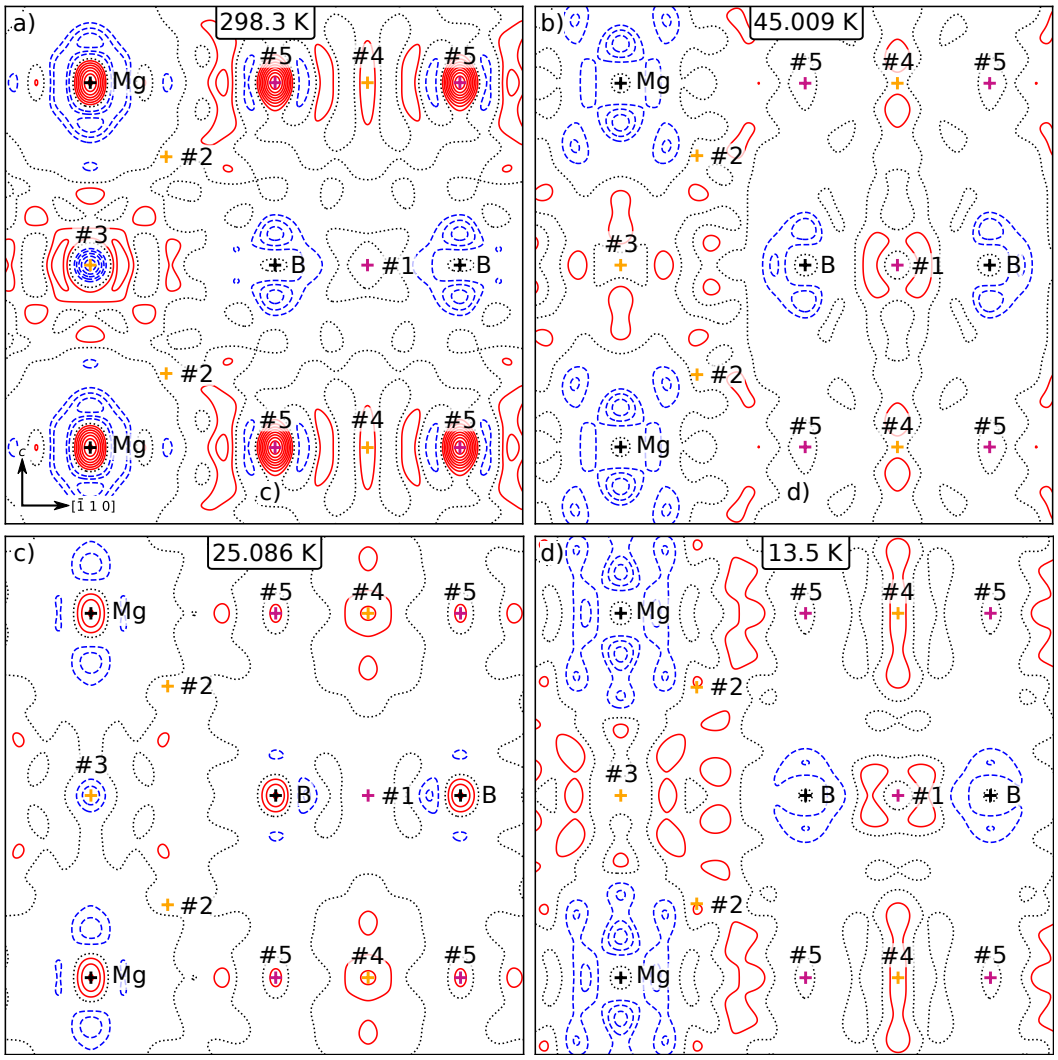

Figure S13: Residual electron density maps for SHC multipolar models refined using experimental XRD data collected at temperatures between a) 298.3(1) K and d) 13.5(5) K (Tab. S7 and Tab. S8). Maps are oriented perpendicular to the hexagonal boron layers in MgB_2. Iso-contour lines are drawn at ± 0.05 $e{\cdot}\text{Å}^{-3}$ using solid red lines for positive, dotted black lines for zero and dashed blue lines for negative values of the residual electron density, respectively.

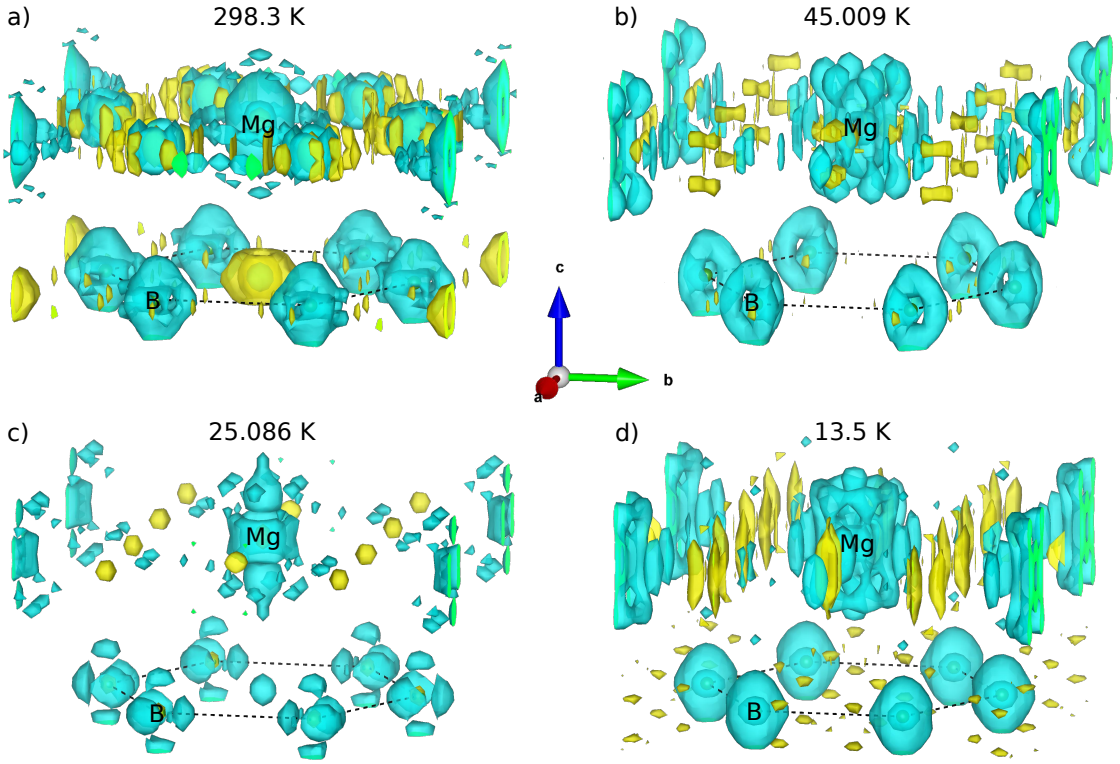

Figure S14: Iso-surface plots of the residual electron density for SHC multipolar models refined using experimental XRD data collected at temperatures between a) 298.3(1) K and d) 13.5(5) K (Tab. S7 and Tab. S8). Iso-surfaces are plotted at $\pm 0.08\ e{\cdot}\text{Å}^{-3}$ using yellow and turquoise colors for positive and negative values of the residual electron density, respectively.

QTAIM analyses

Topological characteristics

CP #	model	T [K]	rank	pos. x y z	$\rho(\mathbf{r}_c)$ [e·Å^{-3}]	$\nabla^2\rho(\mathbf{r}_c)$ [e·Å^{-5}]	ϵ	H λ_1 λ_2 λ_3
1	EHC[a]	100(2)	$(3,-1)$	0.5 0.5 0	0.80	-3.30	0.2	-3.02 -2.43 2.15
	SHC	298.3(1)	$(3,-1)$	0.5 0.5 0	0.85	-5.41	0.3	-3.10 -2.47 0.16
	SHC	45.009(7)	$(3,-1)$	0.5 0.5 0	0.84	-5.23	0.3	-3.05 -2.41 0.23
	SHC	25.086(5)	$(3,-1)$	0.5 0.5 0	0.86	-5.56	0.3	-3.25 -2.57 0.26
	SHC	13.5(5)	$(3,-1)$	0.5 0.5 0	0.87	-5.79	0.3	-3.40 -2.64 0.25
	Ref. S3	RT	$(3,-1)$	0.5 0.5 0	0.81	-4.63	0.3	-3.52 -2.70 1.59
	DFT[b]	–	$(3,-1)$	0.5 0.5 0	0.82	-4.93	0.2	-3.30 -2.87 1.25
	EHC[c]	–	$(3,-1)$	0.5 0.5 0	0.81	-3.79	0.2	-3.20 -2.75 2.16

CP #	**model**	T [K]	**rank**	**pos.** x y z	$\rho(\mathbf{r}_c)$ [e·Å^{-3}]	$\nabla^2\rho(\mathbf{r}_c)$ [e·Å^{-5}]	ϵ	H λ_1 λ_2 λ_3
2	EHC[a]	100(2)	$(3,-1)$	0.865 0.135 0.305	0.19	1.94	168	-0.74 -0.01 2.68
	SHC	298.3(1)	$(3,+1)$	0.863 0.137 0.297	0.15	2.21	–	-0.40 0.03 2.58
	SHC	45.009(7)	$(3,+1)$	0.862 0.138 0.301	0.15	2.27	–	-0.41 0.02 2.66
	SHC	25.086(5)	$(3,+1)$	0.862 0.139 0.300	0.14	2.24	–	-0.41 0.03 2.62
	SHC	13.5(5)	$(3,+1)$	0.863 0.137 0.297	0.15	2.17	–	-0.39 0.03 2.53
	Ref. S3	RT	$(3,-1)$	0.894 0.106 0.253	0.19	1.47	26	-0.27 -0.01 1.75
	DFT[b]	–	$(3,+1)$	0.868 0.132 0.294	0.17	1.97	–	-0.39 0.00 2.36
	EHC[c]	–	$(3,+1)$	0.867 0.133 0.295	0.17	1.90	–	-0.41 0.00 2.31

CP #	**model**	T [K]	**rank**	**pos.** x y z	$\rho(\mathbf{r}_c)$ [e·Å^{-3}]	$\nabla^2\rho(\mathbf{r}_c)$ [e·Å^{-5}]	ϵ	H λ_1 λ_2 λ_3
3	EHC[a]	100(2)	$(3,+1)$	0 0 0	0.06	1.80	–	-0.02 0.91 0.91
	SHC	298.3(1)	$(3,+1)$	0 0 0	0.09	1.31	–	-0.07 0.69 0.69
	SHC	45.009(7)	$(3,+1)$	0 0 0	0.08	1.39	–	-0.06 0.72 0.72
	SHC	25.086(5)	$(3,+1)$	0 0 0	0.08	1.36	–	-0.05 0.70 0.70
	SHC	13.5(5)	$(3,+1)$	0 0 0	0.09	1.22	–	-0.05 0.64 0.64
	Ref. S3	RT	$(3,+1)$	0 0 0	0.17	0.77	–	-0.05 0.41 0.41
	DFT[b]	–	$(3,+1)$	0 0 0	0.10	1.13	–	-0.01 0.57 0.57
	EHC[c]	–	$(3,+1)$	0 0 0	0.10	1.16	–	-0.04 0.60 0.60

CP #	**model**	T [K]	**rank**	**pos.** x y z	$\rho(\mathbf{r}_c)$ [e·Å^{-3}]	$\nabla^2\rho(\mathbf{r}_c)$ [e·Å^{-5}]	ϵ	H λ_1 λ_2 λ_3
4	EHC[a]	100(2)	$(3,+1)$	0.5 0.5 0.5	0.07	0.90	–	-0.02 0.14 0.78
	SHC	298.3(1)	$(3,+1)$	0.5 0.5 0.5	0.10	0.40	–	-0.09 0.01 0.47
	SHC	45.009(7)	$(3,+1)$	0.5 0.5 0.5	0.10	0.40	–	-0.10 0.02 0.49
	SHC	25.086(5)	$(3,+1)$	0.5 0.5 0.5	0.10	0.40	–	-0.09 0.01 0.48
	SHC	13.5(5)	$(3,+1)$	0.5 0.5 0.5	0.10	0.40	–	-0.09 0.01 0.47
	Ref. S3	RT	$(3,+1)$	0.5 0.5 0.5	0.10	0.39	–	-0.04 0.03 0.40
	DFT[b]	–	$(3,+1)$	0.5 0.5 0.5	0.11	0.38	–	-0.05 0.01 0.42
	EHC[c]	–	$(3,+1)$	0.5 0.5 0.5	0.10	0.41	–	-0.03 0.00 0.44

CP #	**model**	T [K]	**rank**	**pos.** x y z	$\rho(\mathbf{r}_c)$ [e·Å^{-3}]	$\nabla^2\rho(\mathbf{r}_c)$ [e·Å^{-5}]	ϵ	H λ_1 λ_2 λ_3
5	EHC[a]	100(2)	$(3,+3)$	0.667 0.333 0.5	0.07	0.87	–	0.04 0.04 0.79
	SHC	298.3(1)	$(3,-1)$	0.667 0.333 0.5	0.10	0.41	0.00	-0.04 -0.04 0.49
	SHC	45.009(7)	$(3,-1)$	0.667 0.333 0.5	0.10	0.42	0.00	-0.05 -0.05 0.52
	SHC	25.086(5)	$(3,-1)$	0.667 0.333 0.5	0.10	0.42	0.00	-0.04 -0.04 0.50
	SHC	13.5(5)	$(3,-1)$	0.667 0.333 0.5	0.10	0.41	0.00	-0.04 -0.04 0.49
	Ref. S3	RT	$(3,-1)$	0.667 0.333 0.5	0.11	0.41	0.00	-0.04 -0.04 0.49
	DFT[b]	–	$(3,-1)$	0.667 0.333 0.5	0.11	0.44	0.00	-0.01 -0.01 0.45
	EHC[c]	–	$(3,-1)$	0.667 0.333 0.5	0.11	0.45	0.00	-0.01 -0.01 0.47

CP #	**model**	T [K]	**rank**	**pos.** x y z	$\rho(\mathbf{r}_c)$ [e·Å^{-3}]	$\nabla^2\rho(\mathbf{r}_c)$ [e·Å^{-5}]	ϵ	H λ_1 λ_2 λ_3
6	EHC[a]	100(2)	$(3,+1)$	0.766 0 0.305	0.19	1.93	–	-0.74 0.00 2.67
	SHC	298.3(1)	$(3,-1)$	0.763 0 0.298	0.15	2.23	13	-0.40 -0.03 2.66
	SHC	45.009(7)	$(3,-1)$	0.760 0 0.302	0.15	2.28	16	-0.41 -0.02 2.71
	SHC	25.086(5)	$(3,-1)$	0.760 0 0.301	0.15	2.25	13	-0.41 -0.03 2.69
	SHC	13.5(5)	$(3,-1)$	0.763 0 0.298	0.15	2.19	11	-0.39 -0.03 2.61
	Ref. S3	RT	$(3,+1)$	0.816 0 0.246	0.19	1.47	26	-0.28 0.01 1.74
	DFT[b]	–	$(3,-1)$	0.771 0 0.294	0.17	1.97	1697	-0.39 -0.00 2.36
	EHC[c]	–	$(3,-1)$	0.771 0 0.294	0.17	1.89	282	-0.41 -0.00 2.31

Table S9: Selected critical points (CP) as obtained from a QTAIM analysis of the electron density distribution $\rho(\mathbf{r})$ in MgB_2. Values were obtained from multipolar refinements based on the experimental XRD data and the static theoretical structure factors in this paper, from Tsirelson *et al.*,[S3] and from a periodic DFT calculation. [a]model E-EHCM1 in Tab. S6; [b]unit cell parameters taken from E-EHCM1; [c]model T-EHCM1 in Tab. S5.

Laplacian maps

SHC models using temperature-dependent experimental XRD data

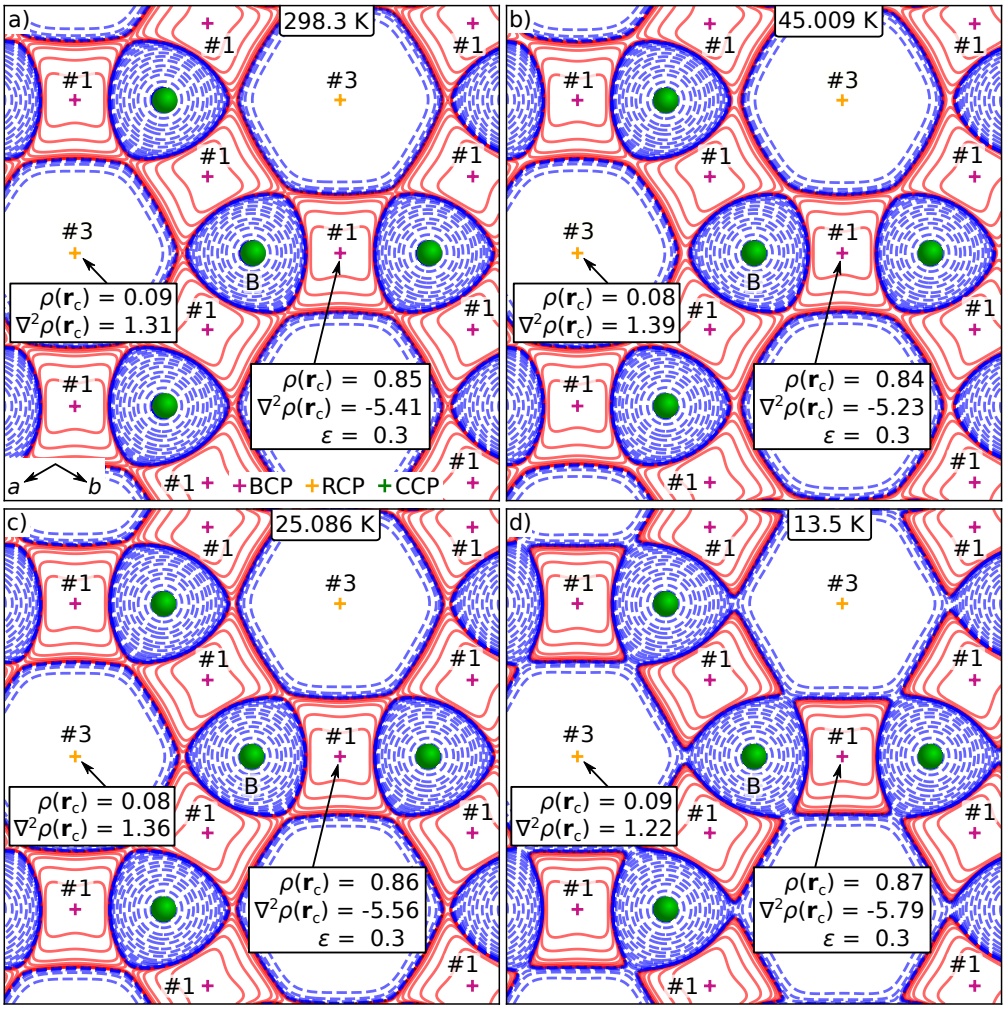

Figure S15: Maps of the Laplacian of the electron density, $\nabla^2\rho(\mathbf{r})$, in the boron network parallel to the a-b plane. The underlying $\rho(\mathbf{r})$ were obtained from SHC multipolar models (Tab. S7 and Tab. S8) refined using experimental XRD data collected at various temperatures between a) 298.3(1) K and d) 13.5(5) K. Contour lines are drawn for negative (solid red lines) and positive values of $\nabla^2\rho(\mathbf{r})$ (dashed blue lines) at levels of $\pm 2 \cdot 10^n$, $\pm 4 \cdot 10^n$, and $\pm 8 \cdot 10^n$ with $n \in \{-2, \ldots, 3\}$. Values of the electron density $\rho(\mathbf{r}_c)$ (in $e{\cdot}\text{Å}^{-3}$), the Laplacian $\nabla^2\rho(\mathbf{r}_c)$ (in $e{\cdot}\text{Å}^{-5}$), and the bond ellipticity (only for BCPs) are specified at the locations of critical points (indicated by crosses). Their numbering refers to Tab. S9.

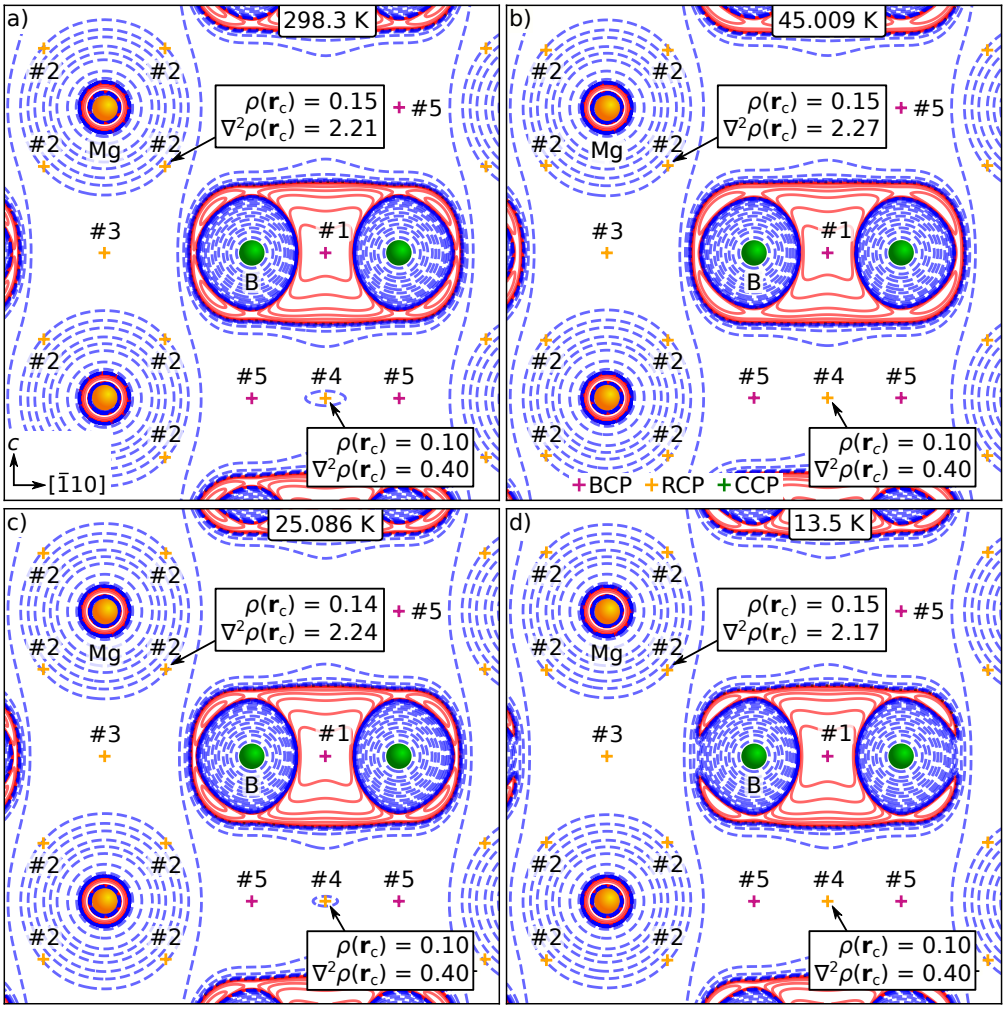

Figure S16: Maps of the Laplacian of the electron density, $\nabla^2\rho(\mathbf{r})$, in a plane containing magnesium and boron atoms. The underlying $\rho(\mathbf{r})$ were obtained from SHC multipolar models (Tab. S7 and Tab. S8) refined using experimental XRD data collected at various temperatures between a) 298.3(1) K and d) 13.5(5) K. Contour lines are drawn for negative (solid red lines) and positive values of $\nabla^2\rho(\mathbf{r})$ (dashed blue lines) at levels of $\pm 2 \cdot 10^n$, $\pm 4 \cdot 10^n$, and $\pm 8 \cdot 10^n$ with $n \in \{-2, \ldots, 3\}$. Values of the electron density $\rho(\mathbf{r}_c)$ (in $e{\cdot}\text{Å}^{-3}$), the Laplacian $\nabla^2\rho(\mathbf{r}_c)$ (in $e{\cdot}\text{Å}^{-5}$), and the bond ellipticity (only for BCPs) are specified at the locations of critical points (indicated by crosses). Their numbering refers to Tab. S9.

Ab-initio ADP values

T [K]	U_{11}(Mg) [Å^2]	U_{33}(Mg) [Å^2]	U_{11}(B) [Å^2]	U_{33}(B) [Å^2]
298.3	0.00488	0.00511	0.00365	0.00520
45.009	0.00260	0.00263	0.00275	0.00351
25.086	0.00258	0.00261	0.00273	0.00349
13.5	0.00258	0.00260	0.00273	0.00348

Table S10: Ab-initio ADP values as derived from lattice dynamic DFT calculations using the finite-difference approach at temperatures corresponding to the conducted low-temperature XRD studies.

Electron density decomposition

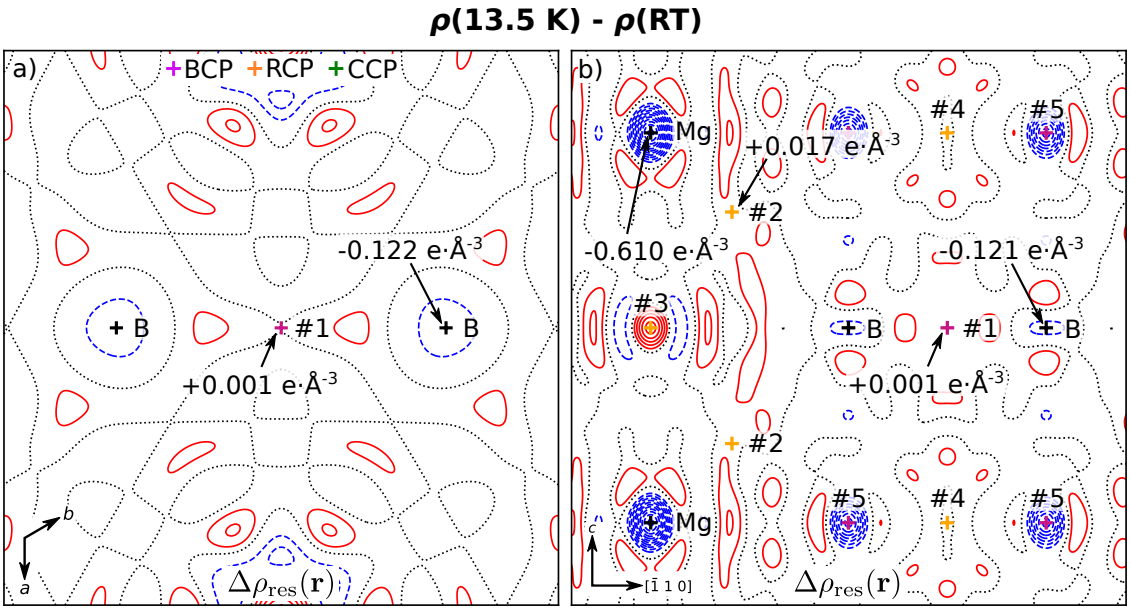

Figure S17: Iso-contour maps of the residual differences between electron density distributions at 13.5 K and RT in planes a) parallel and b) perpendicular to the hexagonal boron layers in MgB_2. Contour lines at positive (red; solid), zero (black; dotted) and negative values (blue; dashed lines) are equally spaced by increments of $\pm 0.05\ e{\cdot}\text{Å}^{-3}$. Crosses indicate the location of the QTAIM critical points specified in Tab. S9.

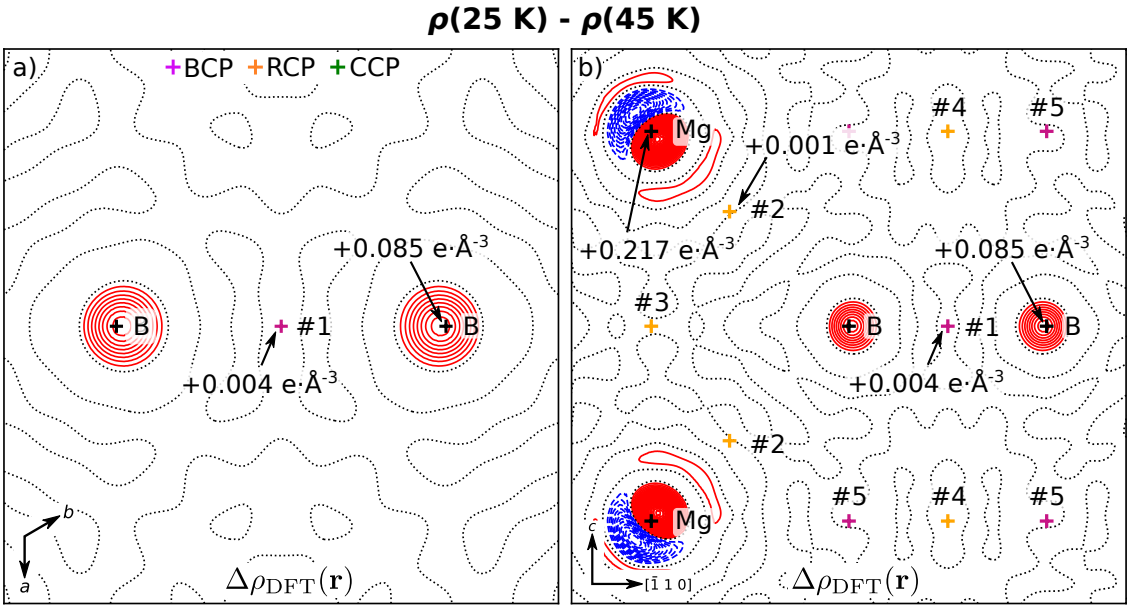

Figure S18: Iso-contour maps of the total differences between electron density distributions at 25 K and 45 K as derived by standard DFT calculations. Maps are oriented a) parallel and b) perpendicular to the hexagonal boron layers in MgB_2. Contour lines at positive (red; solid), zero (black; dotted) and negative values (blue; dashed lines) are equally spaced by increments of $\pm\mathbf{0.01}$ $e{\cdot}\text{Å}^{-3}$. Crosses indicate the location of the QTAIM critical points specified in Tab. S9.

References

(S1) Duisenberg, A. J. M.; Kroon-Batenburg, L. M. J.; Schreurs, A. M. M. An intensity evaluation method: *EVAL*-14. *J. Appl. Cryst.* **2003**, *36*, 220–229.

(S2) Krause, L.; Herbst-Irmer, R.; Sheldrick, G. M.; Stalke, D. Comparison of silver and molybdenum microfocus X-ray sources for single-crystal structure determination. *J. Appl. Cryst.* **2015**, *48*, 3–10.

(S3) Tsirelson, V.; Stash, A.; Kohout, M.; Rosner, H.; Mori, H.; Sato, S.; Lee, S.; Yamamoto, A.; Tajima, S.; Grin, Y. Features of the electron density in magnesium diboride: reconstruction from X-ray diffraction data and comparison with TB-LMTO and FPLO calculations. *Acta Cryst.* **2003**, *B59*, 575–583.